Diploma Thesis

FEM-Modeling of Composite Laminates considering Free Edge Effects

carried out for the purpose of obtaining the degree of
Master of Science (MSc. or Dipl.-Ing. or DI.) submitted at TU Wien,
Faculty of Mechanical and Industrial Engineering, by

Christoph Riepl, BSc.
Matr.Nr.: 01228966

under the supervision of

Associate Prof. Dipl.-Ing. Dr.techn. **Heinz Pettermann**

Associate Prof. Dipl.-Ing. Dr.in techn. **Melanie Todt**

Institute of Lightweight Design and Biomechanics, E317
Research Unit Lightweight Design
TU Wien
Gumpendorferstraße 7/Objekt 8, 1060 Vienna, Austria

Vienna, May 2023

I confirm, that going to press of this thesis needs the confirmation of the examination committee.

Affidavit

I declare in lieu of oath, that I wrote this thesis and performed the associated research myself, using only literature cited in this volume. If text passages from sources are used literally, they are marked as such. I confirm that this work is original and has not been submitted elsewhere for any examination, nor is it currently under consideration for a thesis elsewhere.

I acknowledge that the submitted work will be checked electronically-technically using suitable and state-of-the-art means (plagiarism detection software). On the one hand, this ensures that the submitted work was prepared according to the high-quality standards within the applicable rules to ensure good scientific practice "Code of Conduct" at the TU Wien. On the other hand, a comparison with other student theses avoids violations of my personal copyright.

Vienna, 25th May, 2023

City and Date

Signature

Kurzfassung

Das Ziel der vorliegenden Arbeit ist die Verbesserung der numerischen Modellierung im Bereich der Faserverbundwerkstoffe. Dazu wird der freie Randeffekt in Faserverbundwerkstoffen im Detail untersucht. Bis heute sind exakte analytische Lösungen nur für vereinfachte Modelle für diesen Effekt verfügbar. Numerische Methoden wie die Finite-Elemente-Methode (FEM) können verwendet werden, um Näherungslösungen zu erhalten, sind aber aufgrund des hohen Rechenaufwands für vernünftige Ergebnisse auf einfache Geometrien und Randbedingungen beschränkt.

Daher wird in dieser Diplomarbeit der Stacked-Shell-Ansatz angewendet, um zu untersuchen, ob er zur Erfassung des triaxialen Spannungszustands an den freien Rändern von Verbundlaminaten verwendet werden kann. Im Vergleich zu Kontinuumsmodellen würde dieser Ansatz Rechenressourcen einsparen und die Lösung komplexerer Modelle ermöglichen. Beim Stacked-Shell-Ansatz wird jede einzelne Composite-Lage durch eine Schicht von Schalenelementen diskretisiert. Die Interfaces zwischen den einzelnen Lagen werden mit Kohäsiv-Elementen diskretisiert und mit einem Kohäsivzonenmodellansatz kombiniert. Die Schalen- und Kohäsiv-Elemente sind durch das Teilen von Knoten miteinander verbunden.

Die zum Verständnis des Stacked-Shell-Ansatzes notwendigen theoretischen Grundlagen werden erläutert. Dazu gehören die klassische Laminattheorie sowie die Mindlin-Reissner-Schalentheorie und die Grundlagen der Kohäsivzonenmodellierung mit Kohäsivelementen.

Es wird erläutert, wie der Stacked-Shell-Ansatz in eine kommerzielle FEM-Software, wie Abaqus, implementiert werden kann. Anhand zweier Modelle wird die Eignung des Stacked-Shell-Ansatzes für die Simulation von freien Randeffekten untersucht. Das erste Modell, ein kurzer Biegebalken, wird verwendet, um die Fähigkeit des Stacked-Shell-Ansatzes zu zeigen, die transersalen Schubspannungen genau zu erfassen und den Einfluss der kohäsiven Interfaceeigenschaften zu zeigen. Das zweite Modell ist eine Faserverbundschale mit freien Rändern, die mit Verschiebungen belastet wird. Die Ergebnisse dieses Modells werden verwendet, um die erforderliche Netzgröße und die Gesamtqualität der Ergebnisse im Bereich der freien Ränder zu bewerten. Daher werden die Ergebnisse der Modelle mit Referenzmodellen unter Verwendung von Kontinuumselementen verglichen und interpretiert.

Diese Arbeit zeigt, dass der Stacked-Shell-Ansatz in der Lage ist, die interlaminaren Spannungen am freien Rand von geschichteten Faserverbundlaminaten mit guter Übereinstimmung im Vergleich zu rechenaufwändigeren Kontinuumsmodellen zu erfassen.

Abstract

The aim of the present work is to improve the numerical modeling in the field of layered composites. For this purpose, the free edge effect in layered composites is investigated in detail. Until today, exact analytical solution are only available for simplified models for this effect. Numerical methods like the Finite Element Method (FEM) can be used to obtain approximate solutions, but are limited to simple geometries and boundary conditions, due to high computational demands for reasonable results.

Therefore, in this master thesis, the Stacked Shell Approach is applied to investigate whether it can be used to capture the triaxial stress state at composite laminates' free edges. Compared to continuum models, this approach would save computational resources, allowing for more complex models to be solved. The Stacked Shell Approach discretizes every individual composite ply with a layer of shell elements. The interfaces between the single layers are discretized using a cohesive zone model approach in combination with cohesive elements. The shell and cohesive elements are connected by sharing nodes.

The theoretical foundations necessary to understand the Stacked Shell Approach are explained. These include the classical laminate plate theory, as well as the Mindlin-Reissner shell theory and the basics of cohesive zone modeling with cohesive elements. Details how the Stacked Shell Approach can be implemented in a commercial FEM software, like Abaqus are given. Two models are used to evaluate the suitability of the Stacked Shell Approach for simulating free edge effects. The first model, a

short bending beam, is used to show the capability of the Stacked Shell Approach to capture the transverse shear stresses accurately and assess the influence of the cohesive interface properties. The second model is a composite shell with free edges, loaded with displacements. The results of this model are used to evaluate the necessary mesh size, and the overall quality of the results in the free edge region. Therefore, the results of the models are compared to reference models using continuum elements and interpreted.

This work shows that the Stacked Shell Approach is able to capture the interlaminar stresses at the free edge of layered composites with good agreement compared to computationally more expensive continuum models.

Table of Contents

Kurzfassung i

Abstract iii

1 Introduction 1
- 1.1 Background . . . 1
- 1.2 Motivation . . . 4

2 Literature Review 6

3 Theoretical Principles 11
- 3.1 Failure Mechanisms in Composites . . . 11
  - 3.1.1 Free Edge Effect . . . 14
  - 3.1.2 Onset and growth of delamination . . . 15
- 3.2 Classical Laminate Plate Theory for Layered Materials . . . 18
- 3.3 Stacked Shell Approach . . . 22
  - 3.3.1 Shell Elements . . . 23
  - 3.3.2 Cohesive Elements . . . 25
  - 3.3.3 Traction-separation Law . . . 30

4 Application of the SSA 32
- 4.1 SSA modelling . . . 32
- 4.2 Stress evaluation at the free edge . . . 34
- 4.3 Transverse shear model . . . 36
  - 4.3.1 SSA model . . . 36
  - 4.3.2 Reference model . . . 38
- 4.4 Free edge effect model . . . 38
  - 4.4.1 SSA model . . . 40
  - 4.4.2 Reference model . . . 41

5 Results **42**
5.1 Transverse shear model 42
5.2 FEE model 46
5.2.1 Cross-Ply Laminates 46
5.2.2 Angle-Ply Laminates 54

6 Conclusion **58**

A Stress Evaluation with A2M **60**

Bibliography **65**

List of Abbreviations

A2M Abaqus2Matlab

CAE Computer Aided Engineering

CE cohesive element

CFRP carbon fiber reinforced plastics

CLPT Classical Laminate Plate Theory

CZM cohesive zone modeling

DOF degrees of freedom

FEE free edge effect

FEM finite element method

FRP fiber reinforced plastics

GUI graphical user interface

LEFM Linear Elastic Fracture Mechanics

SSA Stacked Shell Approach

TSL traction-separation law

UD unidirectional

VCCT Virtual Crack Closure Technique

List of Figures

1.1 Airbus A350 XWB material shares by weight . . . 3
1.2 Schematic visualization of the Stacked Shell Approach . . . 5

3.1 Internal failure mechanisms of composites . . . 12
3.2 Interlaminar stress at layer interface of angle-ply laminate . . . 16
3.3 Linear damage evolution . . . 17
3.4 Exponential damage evolution . . . 17
3.5 Laminate with n-layers . . . 18
3.6 Local and global reference coordinate systems . . . 18
3.7 Mindlin-Reissner shear deformation theory . . . 25
3.8 Generic cohesive law for cohesive zone modeling (CZM) . . . 27
3.9 Standard 3d 8-node cohesive element (CE) . . . 28
3.10 Parent domain of CE . . . 28
3.11 Shape functions N_i of CE . . . 29

4.1 SSA assembly of a cohesive element with two shell elements . . . 33
4.2 Schematic visualization of stress evaluation for cohesive elements . . . 35
4.3 Simulation setup for transverse shear model . . . 36
4.4 FEE model setup and location for interlaminar stress results . . . 39

5.1 Deflection of transverse shear beam . . . 43
5.2 Normal stress σ_{xx} of transverse shear beam . . . 44
5.3 Shear stress σ_{xz} of transverse shear beam . . . 44
5.4 Shear stress σ_{xz} of transverse shear beam . . . 45
5.5 Effect of element size for layup A Layup A - σ_{zz} at Interface 1 . . . 47
5.6 Effect of element size for layup A Layup A - σ_{yz} at Interface 1 . . . 48
5.7 Layup A - σ_{xx} of ply 1 (0°) at Interface 1 . . . 48
5.8 Layup A - σ_{xx} of ply 2 (90°) at Interface 1 . . . 49
5.9 Layup A - σ_{yy} of ply 1 and 2 at Interface 1 . . . 49
5.10 Layup B - σ_{zz} and σ_{yz} at Interface 1 . . . 50

5.11 Layup B - σ_{xx} of ply 1 (90°) at Interface 1 51
5.12 Layup B - σ_{xx} of ply 2 (0°) at Interface 1 51
5.13 Layup B - σ_{yy} of ply 1 and 2 at Interface 1 52
5.14 Layup C - σ_{zz} and σ_{yz} at Interface 1 53
5.15 Layup D - σ_{zz} and σ_{yz} at Interface 1 54
5.16 Layup D - σ_{xz} at Interface 1 55
5.17 Layup E - σ_{zz} and σ_{yz} at Interface 1 56
5.18 Layup E - σ_{xz} at Interface 1 57

List of Symbols

Symbol	Meaning
Chapter	**3**
σ_{tt}, τ_{lt}, τ_{qt}	Interlaminar normal and shear stresses
$\sigma_{tt\mathrm{u}}$, $\tau_{lt\mathrm{u}}$, $\tau_{qt\mathrm{u}}$	Tensile fracture stresses and out-of-plane fracture shear stress
$\sigma_{ij}^{\mathrm{avg}}$	Averaged stress values
X^{avg}	Edge width influenced by free edge effect
δ_m^f	effective displacement at complete failure
δ_m^0	effective displacement at damage initiation
x, y, z	Cartesian coordinates
l, q, t	Local coordinates
α	Fiber angle
u, v, w	Displacements in x, y, z-Direction
$\boldsymbol{E}$	Elasticity matrix
$\boldsymbol{T}$	Transformation matrix
$\boldsymbol{\sigma}$, σ_{ij}	Cauchy stress tensor with stress components
$\boldsymbol{\varepsilon}$, ε_{ii}	Strain tensor with strain components
γ_{ij}	Shear strain ij
N_x, N_y, N_{xy}	Force resultants
M_x, M_y, M_{xy}	Moment resultants
κ_{ij}	Plate curvatures of reference plane
$\boldsymbol{A}$, $\boldsymbol{B}$, $\boldsymbol{D}$	Extensional, bending and coupling stiffness matrices
t_{p}	Ply thickness
γ_{xy}	Shear angle
φ, ψ	Rotational variables for the plate normal vector
σ_{xz}, σ_{yz}	Transverse shear stresses
$E_{S(k)}$	Submatrix relating transverse shear strains to transverse shear stresses
κ_S	Shear correction factor

Symbol	Meaning
Δ_a	Element length
Δ_i	Relative displacements
$u_{ki}^{+/-}$	Displacements of top(+)/bottom(-) nodes
N_k	Lagrangian shape functions
$\boldsymbol{x}_i$	Global position vector for cohesive element
$\boldsymbol{v}_n$, $\boldsymbol{v}_s$, $\boldsymbol{v}_t$	Local normal and tangential vectors for cohesive element
θ_{si}	Transformation tensor
$\boldsymbol{K}$	Element stiffness matrix
$\hat{\boldsymbol{E}}$	Interface elasticity matrix
$\boldsymbol{t}$	Nominal traction vector
t_n, t_s, t_t	Nominal normal and shear stresses
δ_i	Local separations
t_0	Initial interface thickness
Chapter	**4**
$\tilde{\boldsymbol{E}}$	Interface stiffness matrix
E	Young's modulus
G	Shear modulus
I	Second moment of inertia
ν	Poisson's ratio
κ	Timoshenko shear coefficient
$q(x)$	Distributed load
ζ	Coordinate for result plots

Chapter 1

Introduction

1.1 Background

Lightweight design and the associated potential to reduce weight have played a key role in technology for decades, especially in the aerospace industry. As climate change is progressing, the use of lightweight design is still increasing in the sectors of transportation and mobility, as well as (renewable) energy, as the efficient use of materials, in addition to cost and weight savings, is expected to have immense potential for reducing CO_2 emissions in these sectors. Composite laminates made of fiber reinforced plastics (FRP) are often used for these applications and are therefore becoming increasingly important.

The individual layers or plies of FRP laminates consist of a combination of two or more different types of materials, whose components have clearly identifiable interfaces. These materials can be divided into a reinforcement phase, in the case of FRP the fibers (e.g., carbon, glass, aramid, etc.), and the matrix phase (e.g., plastic, ceramic, metal, etc.) in which the fibers are embedded. This key aspect of these materials allows the material properties to be designed as required, within certain limits, by the material combination, leading to usually far better properties compared to the respective

individual materials. This is one of the main reasons why FRP's have established themselves as an important class of structural materials, especially in lightweight design. Due to their outstanding characteristic values in specific strength and specific stiffness, compared to conventional materials, like aluminum or titanium, and their great flexibility in terms of design possibilities and manufacturing methods, lightweight structures are now one of the primary areas of application for fiber composites.

This is particularly evident in the aerospace sector. Here, increased reliance has been placed on these materials within the last decades. Fifty years ago, the use of modern composite materials was limited to special fighter aircraft, today all aircraft and spacecraft benefit from them. For example, the Airbus A380 (first delivery in 2007) was already made of 28% carbon fiber reinforced plastics (CFRP). For the A350 XWB (first delivery in 2015), the CFRP share was already at 53%, as shown in Figure 1.1. The A350 XWB along with the Boeing 787, were one of the first aircraft with the entire fuselage made from CFRP, demonstrating the immense potential of these materials [2]. It can be assumed that this development will continue in the coming years and that new generations of aircraft will have an even higher carbon content. Airbus, for example, wants to be able to offer the first hydrogen-powered aircraft by 2035 under the motto "Zero Emissions". The pressure vessels required for this will likely be made largely of CFRP. Mainly because weight savings can be achieved compared to metals, but additionally the corrosion resistance is superior.

Likewise in the field of renewable energy sources, the percentage of FRPs used continues to rise. In particular, the development and expansion of wind turbines in recent years would not have been possible without their use. To make wind turbines more powerful and efficient, their diameters are constantly increased, as this makes transport, installation and maintenance of the wind turbines more efficient. The increasing diameters and heights of new wind turbines additionally make it possible to take advantage of stronger air currents at higher altitudes, leading to higher power outputs.

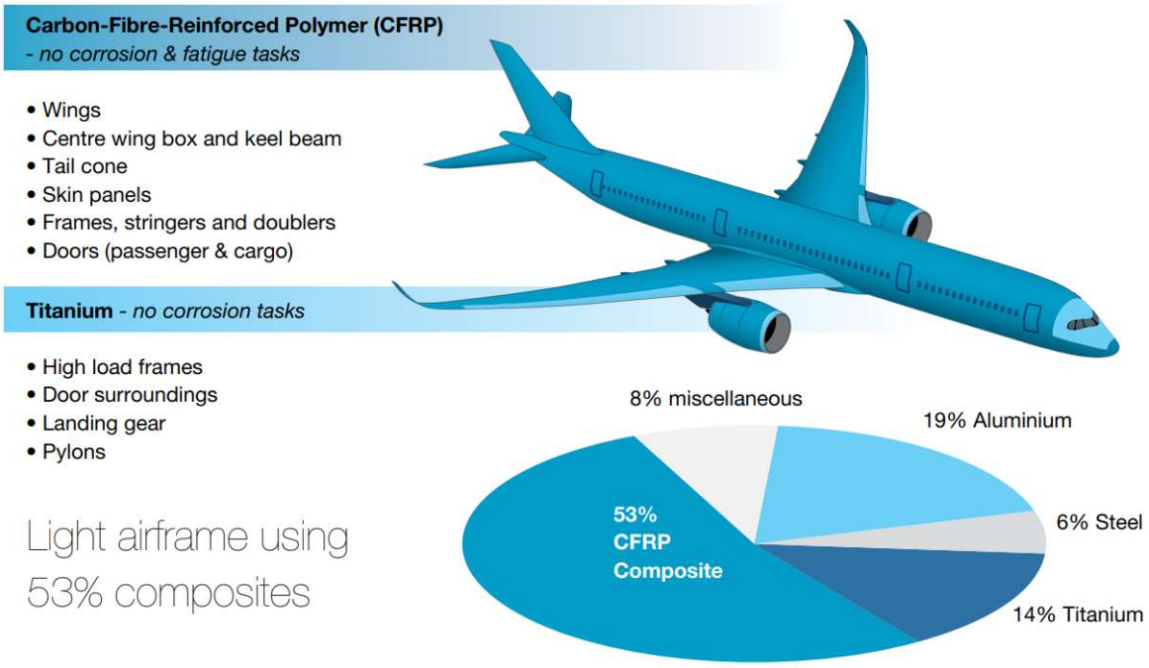

Fig. 1.1: Airbus A350 XWB material shares by weight [2]

This development becomes clear when comparing the average turbine diameter of all wind farms operating in the USA, which is approximately 50 meters, with that of a standard offshore turbine today. These reach a diameter of 220 meters and a total height of up to 260 meters. These new types of turbines are predominantly built from FRP, with mainly carbon and fiberglass as reinforcement materials [30].

To fully exploit the potential of these materials, one of the most important engineering tasks in lightweight design is to precisely calculate the behavior of lightweight structures. Since fiber-reinforced plastics show anisotropic material behavior and weak interfaces due to their layered structure, this task is made quite difficult. Therefore, in recent decades, the finite element method (FEM), supported by Computer Aided Engineering (CAE) programs, has been increasingly used to analyze the complex structural behavior of lightweight structures. This allows simplified models to be used to analyze the complex behavior and failure modes that occur in composites.

The failure modes of laminated composites can be divided into ply failures, so-called intralaminar failure and delamination, so-called interlaminar failure.
Delamination can be further subdivided according to the areas in which it occurs. On the one hand, it can occur at the inner regions of the composite, due to impacts or manufacturing defects (e.g., inclusions, voids), and on the other hand, it can occur due to the high interlaminar stresses at structural discontinuities (ply drops, cut outs) and free edges.
The interlaminar stresses at the free edge are caused primarily by the mismatch of the elastic properties of two adjacent layers [13]. In this thesis a novel simulation approach will be used to try capture these stress concentrations at the free edges of composites, often referred to as "free edge effect (FEE)".

1.2 Motivation

Although numerous papers have been published since about 1970 on the subject of free edge effects in FRPs, there is still a need for more precise and efficient simulation models and solutions. As will be explained in chapter 2, analytical solutions for the free edge effect are usually limited to simple geometries and restricted by necessary assumptions. In comparison, numerical approaches are often limited to models with symmetric laminates and only a few layers due to low computational efficiency. Neither one is useful for potential application areas, such as complex aerospace components. Therefore, this work utilizes an FEM modeling approach, which allows to calculate the triaxial stress state present at free edges in layered laminates. For this purpose, the so-called Stacked Shell Approach (SSA), a layer wise modeling approach, is used in combination with cohesive elements, special purpose finite elements. The individual laminate layers are each discretized by a layer of shell elements with cohesive elements in between, to represent the layer interfaces. This leads to a saving in computational

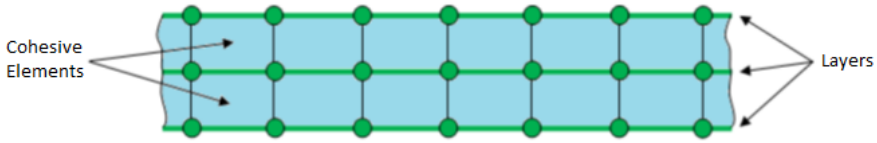

Fig. 1.2: Schematic visualization of the Stacked Shell Approach [23]

resources compared to continuum models and less limitations compared to analytical solutions. A schematic visualization of the SSA can be seen in Figure 1.2.

The goal of this work is to further investigate the applicability and limitations of this approach, which was already pursued in the work of Mayrhofer-Huber [12]. The quality with which the SSA can capture the stress state in the free edge region will be investigated by comparing the results with a reference solution using continuum elements. Furthermore, the necessary mesh size in the free edge region will be investigated and potential problems and limitations of the approach will be pointed out. The results obtained can serve as a basis for further investigations about free edge effects in layered laminates.

Chapter 2

Literature Review

In the past decades, numerous papers have been published about free edge effects in layered structures, attempting to describe the underlying effects either analytically or by numerical modeling. Often these approaches have been supported by experimental results. In this section, some of these studies and the included approaches related to the present work will be briefly reviewed. In addition, work from recent years on the SSA will be presented.

From 1970 to 1974 Pipes and Pagano [21], [17], [16], [20] released most of their pioneering work on free edge effects in composites, which is still referred to by many authors today. In [20] they presented an analytical approach with an approximate elasticity solution for finite-width, angle-ply laminates under uniform uniaxial tension. Although the equilibrium equations are violated in two directions, the solution shows excellent agreement with numerical solutions of that time. To the author's best knowledge, they were also the first ones to connect the influence of the stacking sequence of laminates to the free edge stresses and gave laminate layups with reduced risk of interlaminar failure in [17]. Their numerical solution of the exact analytical equations, using a finite-difference solution in [21], explains the shear transfer mechanism within symmetric laminates, shows the width of the free edge region (approximately equal

to the laminate thickness), and provides excellent results for the displacements and stresses in this area.

Opposed to the displacement-based layer wise approach used in the numerical solutions mentioned above, Pagano [15] used a single-layer approach to calculate the interlaminar normal stress in the mid-plane of a symmetric laminate loaded with uniaxial tension. Compared to his work with Pipes, this approach allows one to consider the influence of the geometric and material parameters of the laminate on the shape of the stress distribution. However, this comes at the cost of the quality of stress approximation through the thickness.

Kassapoglou and Lagace [8], [9] developed a very efficient way to calculate free edge stresses in symmetric laminates under uniaxial tension with the so-called force-balance method. It can be classified as a layer wise stress-based theory. The authors assume stress expressions based on exponential shapes, that the interlaminar stresses must take in order to meet the force and moment equilibrium. By minimizing the laminate complementary energy, the exponential terms of the stress expressions are found. Although there are other stress-based methods, the force-balance method has proven itself highly efficient allowing analysis of thick laminates with up to 100 plies with computational ease. Due to this high efficiency this method has been further refined by several authors. For example, Rose and Herakovich [24] added stress functions, which allow the method to be used in unsymmetrical laminates.

FEEs in composite laminates are mathematically characterized as singularities at the free edge between two dissimilar layers. Therefore, an analytical and a finite element method, dealing with singularities are presented in the next two paragraphs. It shall be noted that this is not a complete overview, as this would not fit the scope of this work. An analytical solution concerning stress singularities in a two-material wedge, was introduced by Hein and Erdogan [7]. The approach uses a Mellin-transformation and the theory of residues. Their solution allows for plane strain or plain stress

problems, to obtain the stresses at the interface and show the dependence on the materials and geometry.

To investigate stress singularities in the vicinity of singular points in structures with geometric discontinuities and anisotropic materials Pageau and Biggers [18] used a two-dimensional finite element formulation. Dividing the region into sectorial elements around the singular point allowed a computationally very efficient formulation of the quadratic shape functions, while showing rapid convergence with several available exact solutions.

Since it is relatively difficult to find an analytical solution, and that these must be constrained by various assumptions, it is not surprising that many researchers have used numerical approaches, like the FEM. Stiftinger [29] for example, used a special purpose finite element to predict the stresses close to free edges in fiber reinforced laminates. The developed four noded shell element is based on an analytical approach and uses modified transverse shear strains to overcome shear locking. A layer wise linear elastic material model is used. The results presented are satisfactory for most configurations, only the interlaminar stress distribution through the thickness could be improved.

A computationally more expensive way is to use three-dimensional elements. Norwood [14] used 32-noded brick elements in his three-dimensional model to calculate the stress fields in symmetric as well as unsymmetric laminates subject to pure mechanical and pure thermal loading. Using a global-local strategy, he calculated the interlaminar stresses at the interfaces within a refined (local) model, which used the displacements calculated by a global model. The interface stresses had to be interpolated and averaged at the Gauss integration points. The results presented by Norwood showed good agreement with other works and will be used as reference in this work.

It can be summarized that analytical approaches are limited to basic geometries and need limiting assumptions, such as symmetric layup or kinematic constraints, whereas

finite element simulations either lack in detail, especially for thick laminates, or are computationally very expensive when three-dimensional models are utilized.

This led to the development of the SSA, a finite element modeling technique for analyzing the behavior of composite structures. The approach was first mentioned by Ladevèze *et al.* [10] in 1998, when proposing a mesomodel for simulating complete fracture phenomena in composites under complex loading conditions. The model is based on the idea that the laminate can be divided into a sequence of stacked homogeneous shell layers throughout the thickness, each representing a single ply, and interlaminar interfaces. These interfaces connect neighboring layers, ensuring stress and displacement transfer between the plies. The mesomodel is capable of predicting the onset and evolution of damage in the laminate, including delamination and matrix cracking, by using a three-dimensional continuum damage mechanics approach. The effectiveness of the mesomodel is demonstrated through comparison with experimental data and other numerical models, including dynamic loading.

The basic idea of this work was also used in [26] to simulate the intermediate velocity impact behavior of woven composite laminates, by using progressive damage models for plies and interfaces. With the used energy-based continuum damage mechanics approach in combination with the SSA, the model is able to cover tensile and compressive ply damage as well as shear damage and plastic deformations. The simulations conducted by Schwab *et al.* [26] were validated by comparing the results with experimental data of a drop test. The study concludes that the SSA with progressive damage model provides a useful tool for designing and optimizing composite structures for improved impact resistance, and that further research is needed to improve the accuracy and efficiency of the model.

The concept of the stacked shell approach is also followed by Lampeas and Fotopoulos [11]. It is the first work using the SSA and focusing on interlaminar stresses in

composites. The effectiveness of the proposed technique in calculating interlaminar stresses of composite structures has been demonstrated through its application to laminated plates subjected to sinusoidally distributed transverse loading, laminated strips under three-point bending, and laminated cylindrical shells under cylindrical bending. The analysis of displacement and both in-plane and out-of-plane stresses indicate that the methodology is highly accurate and efficient.

Chapter 3

Theoretical Principles

In this section the theoretical background necessary to understand and build the used FEM models will be given. First, a compact overview of failure mechanisms in composites is given to show the need for the SSA. To understand the principle of this approach, it is necessary to know how stress calculations are performed in layered materials. Therefore, the commonly used Classical Laminate Plate Theory (CLPT) will be briefly summarized. Since this work uses a layer wise approach with the SSA, in which homogeneous shells are stacked, shell theories, as well as the basic formulation of shell and cohesive elements, are presented.

3.1 Failure Mechanisms in Composites

As mentioned in the introduction, composite materials are widely used in various engineering applications due to their high strength-to-weight ratio and specific properties. However, anisotropy of the material, as well as the complex microstructure of composites, leads to various failure mechanisms, which need to be considered for the design and optimization of composite structures.

The failure criteria of composites can be divided into global and internal failure.

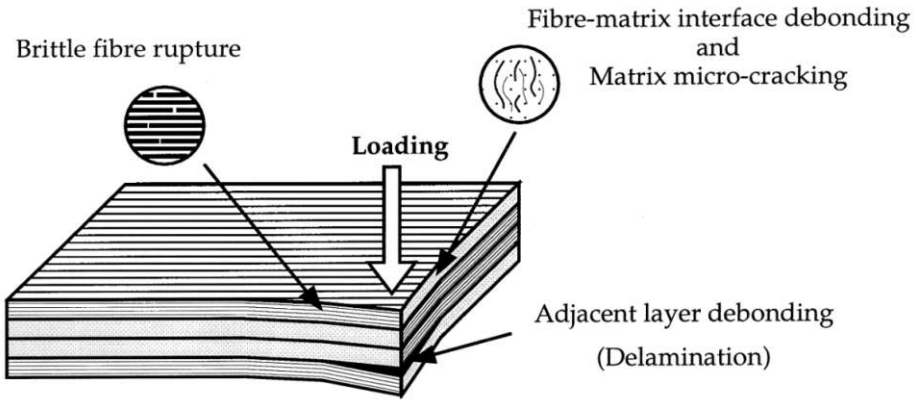

Fig. 3.1: Internal failure mechanisms of composites [10]

Global failure refers to large deformations or global instabilities typical for thin-walled structures (e.g., buckling). These mechanisms will not be discussed in this thesis, more in-depth literature can be found in, e.g., [31]. Internal failures of composites are different types of material failures, which can be further subdivided into intralaminar and interlaminar failure, some of them are illustrated in Figure 3.1. It is important to note that composite materials often have a complex failure behavior and multiple failure mechanisms can occur simultaneously, depending on the specific application, loading, and material behavior. Therefore, the design and analysis of composite structures requires an understanding of all the different failure mechanisms and their interactions.

Intralaminar failure, or ply failure, refers to the failure of the fibers or the matrix within a single ply of a composite structure. It can lead to a significant reduction in strength and stiffness of the structure. There are several types of intralaminar failure in composites, including:

- **Fiber rupture**: When fibers are loaded in tension and the breakage stress is exceeded.
- **Fiber pull-out**: Often occurs in combination with fiber breakage in unidirectional (UD)-laminates under tensile load.

- **Fiber buckling**: Under compressive load, individual fibers or regions of parallel fibers can buckle.
- **Matrix cracking**: Matrix cracking is the failure of the matrix within a single layer of a composite structure. If this happens during loading normal to fiber direction, it is often called transverse cracking.
- **Fiber/matrix debonding**: This is the separation of the fibers from the matrix within a single ply. It can be caused by a variety of factors, but often occurs, when the layer is loaded normal to the fiber direction.

In order to take these failure mechanisms into account in the evaluation of composite structures, various failure criteria have been developed. The maximum stress criterion predicts failure, when one of the stress components in the principal material direction reaches the ultimate strength. A distinction is made between compression and tensile stresses, but the interaction of stresses is not taken into account. The maximum strain criterion is similar, however, by considering the transverse contractions when calculating the distortions, an interaction of the stress components is considered. Probably the best-known criteria are the Tsai-Wu and Tsai-Hill criteria. These are quadratic failure criteria that also take stress interaction into account. If one looks at the failure envelopes of these two criteria, a similarity to the v. Mises yield criterion can be seen. More details on failure mechanisms and criteria can be found in [28].

Interlaminar failure, also called delamination, refers to the separation of individual layers from each other in laminated structures. A distinction can be made as to whether the delamination occurs internally or at a free edge. Internal delamination can be caused by impacts (during manufacturing, maintenance, bird strikes, etc.), in which case the damage might not be visible on the top surface of the laminate, because the delamination occurs between deeper layers and is therefore hard to detect

visually. Other causes are manufacturing defects, such as impurities or gas formation during the curing process, as well as structural discontinuities, occurring with ply drop-offs or bonded or laminated connections. Moisture and temperature can also cause interlaminar stresses that lead to delamination. Fatigue stress is another cause which, due to mechanical or thermal fatigue stresses, can cause matrix cracks to grow up to the interfaces, where they turn into delamination and, in the further course, can grow together with other defects. Both forms of delamination (internal and free edge) can lead to a significant reduction in strength and stiffness and result in failure of the structure. However, this work focuses solely on the interlaminar stresses resulting from the free edge effect, and the capabilities of the SSA to capture these. Therefore, the free edge effect will be discussed in more detail in the next section.

3.1.1 Free Edge Effect

At free edges, which include holes and recesses, of multi-directional laminates a tri-axial stress state occurs, also known as the free edge effect. In these areas the CLPT is not valid (see section 3.9). The interlaminar stresses present in the free edge region can become critical and lead to free edge delamination. It is important to understand that this effect does not emerge due to manufacturing defects but is also present in defect-free components.

Interlaminar normal stresses occur in cross-ply laminates due to the differences in Poisson's ratio, and interlaminar shear stresses occur in angle-ply laminates due to the differences in shear behavior. The magnitude of the occurring stresses depends on how large the differences are in Poisson's ratio and shear behavior, as well as Young's moduli and shear moduli, of adjacent plies. In addition, the laminate layup, thickness, the loads, and the boundary conditions influence the development of the FEE [17]. The effect decreases with increasing distance from the free edge until the

stress values converge to the calculations using CLPT (approximately in distance of laminate thickness). In addition to accurately calculating the free edge effect by simulation, design, and material engineering measures should be considered to prevent the effect in the first place. Among other things, shear-toughened resin, the use of high-strength adhesives in the free edge area, or the application of overlaps can reduce or prevent the occurrence of the free edge effect.

As described in section 2, there are several approaches to determine the interlaminar stresses at the free edge, which can lead to delamination. However, to the author's knowledge, there is no analytical solution that can accurately describe the stress state at the free edge. Various possibilities to approximate the triaxial stress state are summarized in [13]. Among them some analytical approaches can be found, which come to a satisfying solution by means of simplifications and assumptions for simple geometries, as well as various numerical models, which often require a lot of computational effort. A relatively old approach from Pipes and Pagano [21], which has also proven itself in experiments, using a finite difference solution to solve the exact elasticity equations for a symmetric angle-ply laminate, is shown graphically in Figure 3.2.

3.1.2 Onset and growth of delamination

To assess whether there is onset or growth of delamination either fracture mechanics, or cohesive zone modeling (CZM) can be used. Although in this work, the onset and growth of delamination are not considered in the simulation, the possibilities of evaluating the delamination behavior of composites using CZM, shall be briefly discussed. This would allow the SSA to be expanded in a future work.

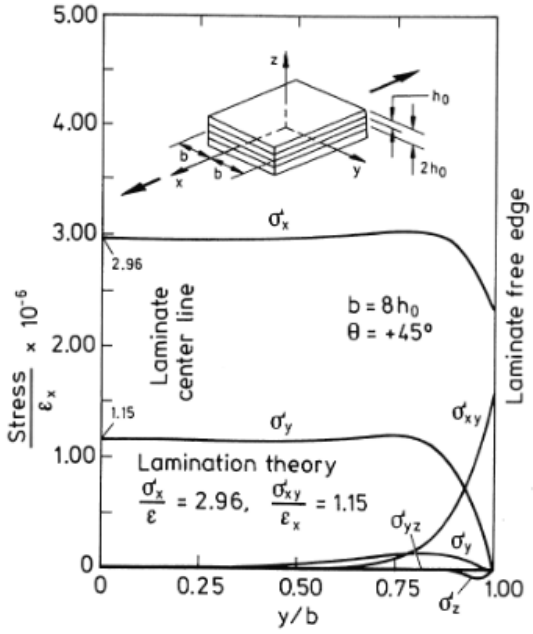

Fig. 3.2: Interlaminar stress at layer interface of angle-ply laminate [21]

With the computed stresses a quadratic stress criterion can be used to assess whether delamination onset occurs. An often used stress criterion is

$$(\frac{\sigma_{tt}}{\sigma_{ttu}})^2 + (\frac{\tau_{lt}}{\tau_{ltu}})^2 + (\frac{\tau_{qt}}{\tau_{qtu}})^2 \geq 1 \quad , \tag{3.1}$$

with σ_{tt} being the interlaminar normal stress, τ_{lt} and τ_{qt} the interlaminar shear stresses. The coefficients σ_{ttu}, τ_{ltu} and τ_{qtu} are the tensile ultimate stress and out-of-plane ultimate shear stresses, respectively. Delamination onset occurs when the inequality in Eqn.(3.1) is satisfied.

It should be noted that the results are significantly affected by the accuracy of the numerical/analytical calculation of the interlaminar stresses. Therefore, the stress

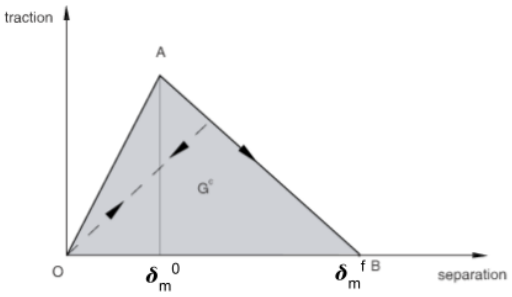

Fig. 3.3: Linear damage evolution [27]

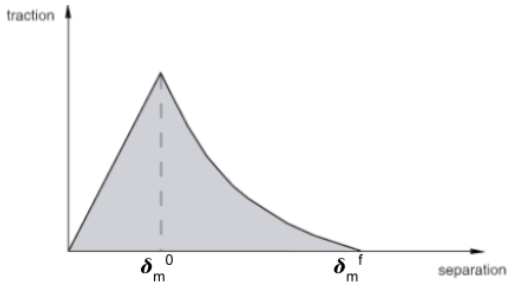

Fig. 3.4: Exponential damage evolution [27]

values in the edge region are often calculated at discrete points, or averaged within the free edge region with

$$\sigma_{ij}^{\text{avg}} = \frac{1}{X^{\text{avg}}} \int_0^{X^{\text{avg}}} \sigma_{ij} \cdot dx \quad , \tag{3.2}$$

where X^{avg} denotes the averaging width, which depends on the decay behavior of the interlaminar stresses in the free edge region and is influenced by the layup, ply material and design details [28].

Additionally to delamination onset, delamination growth can be computed, by defining a damage evolution law. In Figures 3.3/3.4 a linear/exponential damage evolution law is shown schematically. Briefly summarized, it can be said that no change in stiffness occurs until damage initiation at δ_m^0 and then decreases according to the damage evolution law defined until complete failure at δ_m^f. As damage initiation and evolution will not be modeled within this work, please refer to [27] for more details on this topic.

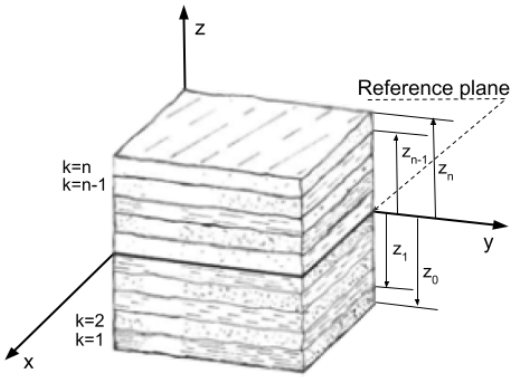

Fig. 3.5: Laminate with n-layers (adopted from [28])

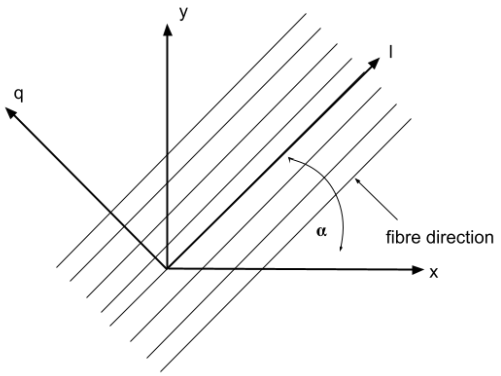

Fig. 3.6: Local and global reference coordinate systems

3.2 Classical Laminate Plate Theory for Layered Materials

The CLPT is one of the most used calculation methods for thin layered composite components. It allows to determine the deformation behavior of thin-walled shell structures under load, as well as the average layer stresses per single ply at any point in the component, as long as the necessary assumptions apply. Using failure criteria, the determined layer stresses (or layer strains) per individual ply are then compared with the corresponding critical material parameters to determine the failure behavior of the fiber composite. In order to make the equations of the CLPT solvable, simplifying assumptions are necessary. Thus, a constant plane stress state is assumed over a single layer thickness **(which does not apply at the free edge)**, and Kirchhoff's-Law is applied. The material properties are assumed to be macroscopic homogeneous and orthotropic for single layers and that plies have linear elastic material behavior. Also, all plies are perfectly bonded between each other.

Formulating Hook's law for layer k of a laminate with n layers (see Figure 3.5) in the reference coordinate system (l, q, t) and transformation to the global reference coordinate system (x, y, z) (see Figure 3.6) leads to

$$\begin{Bmatrix} \sigma_{xx} \\ \sigma_{yy} \\ \tau_{xy} \end{Bmatrix} = (\boldsymbol{T}^{-1})(\boldsymbol{E})_{\mathrm{L}}(\boldsymbol{T}^{-1})^{T} \begin{Bmatrix} \varepsilon_{xx} \\ \varepsilon_{yy} \\ \gamma_{xy} \end{Bmatrix} \quad , \tag{3.3}$$

and can be written in vector form as

$$\boldsymbol{\sigma}^{(k)} = \boldsymbol{E}^{(k)}\boldsymbol{\varepsilon}^{(k)} \quad . \tag{3.4}$$

$\boldsymbol{E}^{(k)}$ is the plane stress elasticity matrix for layer k, which is constant for each layer. $\boldsymbol{T}$ is the transformation matrix and depends on the fiber angle α. Assuming the validity of Kirchhoff's law, the strains ε_{xx}, ε_{yy}, γ_{xy} in the laminate can be written as

$$\begin{Bmatrix} \varepsilon_{xx} \\ \varepsilon_{yy} \\ \gamma_{xy} \end{Bmatrix} = \begin{Bmatrix} \frac{\partial u}{\partial x} \\ \frac{\partial v}{\partial y} \\ \frac{\partial u}{\partial y} + \frac{\partial v}{\partial x} \end{Bmatrix} \quad , \tag{3.5}$$

with the displacements u, v, w of a point P in the laminate. The out-of-plane strains ε_{zz} are neglected, because of the assumptions made beforehand. If the displacements are related to a reference plane (laminate mid plane), Eqn.(3.5) becomes

$$\begin{Bmatrix} \varepsilon_{xx} \\ \varepsilon_{yy} \\ \gamma_{xy} \end{Bmatrix} = \begin{Bmatrix} \frac{\partial u_0}{\partial x} \\ \frac{\partial v_0}{\partial y} \\ \frac{\partial u_0}{\partial y} + \frac{\partial v_0}{\partial x} \end{Bmatrix} - z \begin{Bmatrix} \frac{\partial^2 w_0}{\partial x^2} \\ \frac{\partial^2 v}{\partial y^2} \\ \frac{2\partial^2 w_0}{\partial x \partial y} \end{Bmatrix} \quad , \tag{3.6}$$

with z being the distance of Point P to the reference plane. All variables with index 0 relate to the reference plane. Inserting equation Eqn.(3.6) into Hook's law Eqn.(3.4) leads to

$$\boldsymbol{\sigma}^{(k)} = \boldsymbol{E}^{(k)}\boldsymbol{\varepsilon}^0 - z\boldsymbol{E}^{(k)}\boldsymbol{\kappa} \quad , \tag{3.7}$$

with $\boldsymbol{\varepsilon}^0$ being the strains and $\boldsymbol{\kappa}$ the curvatures of the reference plane.

It is necessary to introduce resulting laminate forces and moments because the stresses within the laminate vary from ply to ply. These stress resultants form a statically equivalent system of forces and moments. The system of three force resultants (N_x, N_y, N_{xy}) and three moment resultants (M_x, M_y, M_{xy}) acting in the midplane is statically equivalent to the current stress distribution across the thickness of the laminate. By integrating the stress components over the thickness of the laminate, these internal forces per length can be calculated. The integral over the total laminate thickness can be replaced by a summation over each single plies thickness. For the moments, the stress components must be multiplied by the distance to the reference plane.

The dimension of these stress resultants is force per length. Inserting Hook's law Eqn.(3.7), already considering the defined strains, consisting of the midplane strains of the plate ε_{ij} and γ_{xy} and the plate curvatures κ_{ij}, which are independent of z, and that $\boldsymbol{E}^{(k)}$ is constant for each layer, the stress resultants can be written as

$$\begin{Bmatrix} N_x \\ N_y \\ N_{xy} \end{Bmatrix} = \sum_{k=1}^{n} \{ \int_{z_k-1}^{z_k} (\boldsymbol{E})^k \begin{Bmatrix} \varepsilon_{xx}^0 \\ \varepsilon_{yy}^0 \\ \gamma_{xy}^0 \end{Bmatrix} dz + \int_{z_k-1}^{z_k} (\boldsymbol{E})^k \begin{Bmatrix} \kappa_{xx} \\ \kappa_{yy} \\ \kappa_{xy} \end{Bmatrix} z dz \} \tag{3.8a}$$

$$\begin{Bmatrix} M_x \\ M_y \\ M_{xy} \end{Bmatrix} = \sum_{k=1}^{n} \{ \int_{z_k-1}^{z_k} (\boldsymbol{E})^k \begin{Bmatrix} \varepsilon_{xx}^0 \\ \varepsilon_{yy}^0 \\ \gamma_{xy}^0 \end{Bmatrix} z dz + \int_{z_k-1}^{z_k} (\boldsymbol{E})^k \begin{Bmatrix} \kappa_{xx} \\ \kappa_{yy} \\ \kappa_{xy} \end{Bmatrix} z^2 dz \} \quad . \tag{3.8b}$$

With the assumption of constant strains and curvature changes per ply, as is permissible for thin layers, these terms can be written in front of the integral. Introducing the matrices $\boldsymbol{A}$, $\boldsymbol{B}$ and $\boldsymbol{D}$, the formulas (3.8a) and (3.8b) can be combined to from the simplified CLPT

$$\begin{Bmatrix} \boldsymbol{N} \\ \boldsymbol{M} \end{Bmatrix} = \begin{Bmatrix} \boldsymbol{A} & \boldsymbol{B} \\ \boldsymbol{B} & \boldsymbol{D} \end{Bmatrix} \begin{Bmatrix} \boldsymbol{\varepsilon}^0 \\ \boldsymbol{\kappa} \end{Bmatrix} \quad . \tag{3.9}$$

These stiffness matrices depend on the material properties of the individual plies and the laminate layup. The extensional stiffness matrix $\boldsymbol{A}$ links normal stresses and strains, as well as shear strains to normal stresses and vice-versa. The bending stiffness matrix $\boldsymbol{D}$ relates the bending moments with the plate curvature. The coupling stiffness matrix $\boldsymbol{B}$ couples normal stress resultants with curvature changes and vice-versa, as well as shear strains to bending stress resultants and twisting strains to normal stress resultants. These coupling effects are new compared to homogeneous isotropic plates, e.g., forces acting in the shell midplane, not only cause distortions (strain/inplane thrust), but also lead to bending deformations or twisting. Likewise, bending and torsional moments cause strains in the reference surface. These and other coupling effects can also affect the stress state and temperature behavior of composite components. Coupling effects can be avoided by selecting a suitable laminate layup. For symmetrical, quasi-orthotropic and quasi-isotropic laminates, all terms of the coupling matrix result to zero, and therefore, no coupling effects are present.

The results of the CLPT provide the global distortions of the laminate related to the global reference coordinate system, or the stresses and strains in each laminate layer k with respect to a local material coordinate system of the single ply. In combination with the failure criteria mentioned before, these results can be used to determine the

deformation and failure behavior of composite structures. A more detailed derivation of the CLPT can be found, e.g., in [28] and [22].

3.3 Stacked Shell Approach

After a brief introduction to the fundamental theories of composites, the Stacked Shell Approach will be explained in detail. The SSA is a finite element modeling approach for analyzing the behavior of laminated composites at the meso level. The composite laminate is divided into a sequence of stacked homogeneous shell layers throughout the thickness, where each shell layer represents a single ply. These shell layers are connected via an interface entity which ensures stress and displacement transfers between adjacent plies. This interlaminar connection can be interpreted as a ply of matrix, whose thickness is negligible compared to the in-plane dimension, and will be referred to as interface.

While the midplane of each ply is discretized by an individual layer of 4-node shell elements, in this work the interfaces between the plies are represented by hexahedral elements with a CZM. Such a cohesive element (CE) shares the nodes of the adjacent shell layers located at the corresponding reference planes. The CEs model the mechanical behavior of the laminate interfaces using a traction-separation based constitutive law. The CEs have a finite geometrical thickness in the used FEM model, equal to the layer thickness t_{p}, since they share nodes with the adjacent shell elements. The interlaminar stresses are captured by the relative displacements of the top and bottom surfaces of the cohesive elements. The in-plane stresses are covered by the shell elements.

Compared to equivalent models discretized by three-dimensional continuum elements, the SSA offers much higher computational efficiency, while still capturing the complex stress state in layered materials. Linearly interpolated continuum elements typically

require small element dimensions and aspect ratios close to one to alleviate the effect of shear locking during bending deformations. In the context of free edge effects, each ply should also be discretized by two or more continuum elements in the thickness direction to describe the possibly nonlinear stress distribution across the ply thickness. Therefore, the number of degrees of freedom (DOF) can be drastically reduced by using shell elements. In addition to this, it should also be possible to increase the element size, but this must first be checked in connection with FEEs.
In the next section, the main components of the SSA, shell and cohesive elements, and related theories are described in detail.

3.3.1 Shell Elements

Shell elements are a type of finite element used to model thin-walled structures, such as plates and shells. They are typically used to model structures whose two dimensions are much larger than the third dimension (thickness), such as thin-walled plates. A general rule of thumb for thin-walled shells is that the thickness is at least 20 times less than the largest dimension. Their volume is reduced to a reference plane by using Kirchhoff-Love or Mindlin-Reissner's theory. This leads to them being less computationally intensive than solid elements, which makes them suitable for large-scale simulations and optimizations. Therefore, they are widely used in many areas of lightweight design, such as aerospace engineering, mechanical engineering, civil engineering, and marine engineering. They can be used to model structures made of various materials, including isotropic, orthotropic, and anisotropic materials. Since curved geometries, as they often occur in lightweight designs, can only be represented faceted with linear shell elements, there are also quadratic and higher-order shell elements, although linear ones usually offer a good approximation, depending on the mesh fineness.

3.3.1.1 Mindlin-Reissner shell theory

In deriving the CLPT, the Kirchhoff-Love shell theory has already been used for Eqn.(3.6). This theory is only valid for very thin plates and shells, since no transverse shear deformation is considered. It can be easily extended to the Mindlin-Reissner plate theory, also known as the theory of first-order shear deformation, which takes into account the effects of transverse shear deformations. This is especially important for thick shells.

By introducing the independent rotation variables φ and ψ for the normal vector of the shell, equation (3.6) changes to

$$\begin{Bmatrix} \varepsilon_{xx} \\ \varepsilon_{yy} \\ \gamma_{xy} \\ \gamma_{xz} \\ \gamma_{yz} \end{Bmatrix} = \begin{Bmatrix} \frac{\partial u}{\partial x} \\ \frac{\partial v}{\partial y} \\ \frac{\partial u}{\partial y} + \frac{\partial v}{\partial x} \\ \frac{\partial u}{\partial z} + \frac{\partial z}{\partial x} \\ \frac{\partial v}{\partial z} + \frac{\partial z}{\partial y} \end{Bmatrix} = \begin{Bmatrix} \frac{\partial u_0}{\partial x} \\ \frac{\partial v_0}{\partial y} \\ \frac{\partial u_0}{\partial y} + \frac{\partial v_0}{\partial x} \\ \frac{\partial z_0}{\partial x} \\ \frac{\partial z_0}{\partial y} \end{Bmatrix} - \begin{Bmatrix} z\frac{\partial \psi}{\partial x} \\ z\frac{\partial \varphi}{\partial y} \\ z(\frac{\partial \psi}{\partial y} + \frac{\partial \varphi}{\partial x}) \\ \psi \\ \varphi \end{Bmatrix} \quad . \tag{3.10}$$

The resultants of the transverse stress components σ_{xz} and σ_{yz} can be written as

$$q_{xz} = \int_{-\frac{t}{2}}^{+\frac{t}{2}} \sigma_{xz} \cdot dz, \quad q_{yz} = \int_{-\frac{t}{2}}^{+\frac{t}{2}} \sigma_{yz} \cdot dz \quad . \tag{3.11}$$

With the equations for transverse shear defined, the equation

$$\boldsymbol{q} = \overline{\boldsymbol{A}}\boldsymbol{\gamma} \tag{3.12}$$

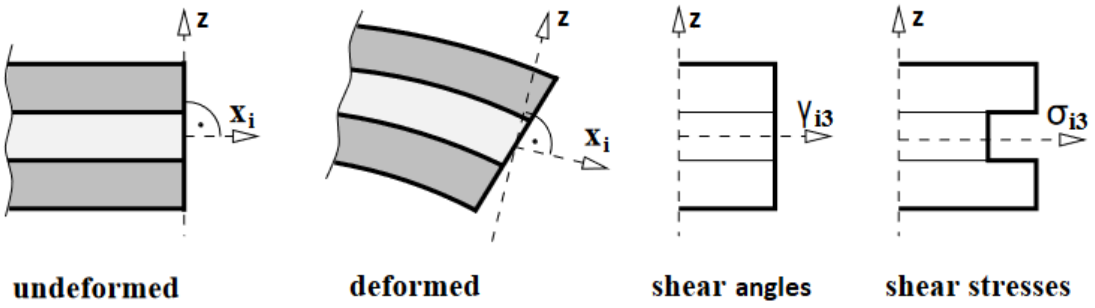

Fig. 3.7: Mindlin-Reissner shear deformation theory [29]

can be added to Eqn.(3.9), with

$$\overline{\boldsymbol{A}} = \sum_{k=1}^{n} \kappa_S \boldsymbol{E}_{S(k)}(z_k - z_{k-1}), \quad \boldsymbol{\gamma} = \begin{Bmatrix} \gamma_{xz} \\ \gamma_{yz} \end{Bmatrix} \quad . \tag{3.13}$$

$\boldsymbol{E}_{S(k)}$ is the 2 x 2 submatrix that relates transverse shear angles to the transverse shear stress components, and κ_S is the shear correction factor ($\frac{5}{6}$ for isotropic and orthotropic shells).

This so called first-order shear deformation theory allows robust results when simulating the structural behavior of thin or moderately thick plates, but it cannot correctly represent the transverse shear stresses. The shear strains are considered to be constant through the thickness, and the shear stresses are non-continuous through the thickness of the plate, see Figure 3.7. There are several approaches to improve the results for transverse shear stresses, whether by using correction factors $\kappa_{S(k)}$, or higher order shear deformation theories with cubic polynomials. A summary of these, and references to more detailed literature, can be found in [29].

3.3.2 Cohesive Elements

As mentioned in section 3.1.1, the interlaminar stresses form a stress singularity at the free edge, quite similar to the stresses at a crack tip. Therefore, it is obvious that

for the calculation of the behavior and the stresses at the free edge, the models of fracture mechanics play a significant role. In fracture mechanics, two methods have been established, the Virtual Crack Closure Technique (VCCT), which is based on Linear Elastic Fracture Mechanics (LEFM), and the CZM approach. The VCCT refers to the method developed by Griffith [6] to predict fracture in brittle materials. The principle of the VCCT as proposed in [25], is that a finite element model of a solid with pairs of coincident nodes coupled together at the crack is used. When a critical value is reached during loading, the coupled nodes are released, and the crack can extend to the next element. The energy released during this crack extension for element length Δa is assumed to be equal to the energy required to close the crack again. The drawback of this method is that a very fine mesh is necessary at the crack tip, and an existing crack must be present in the model [1]. The opening and moving of the crack front are also computationally very demanding. A different approach has therefore been developed based on the cohesive zone concept proposed by Dugdale [5] and Barenblatt [3] with the CZM approach.

3.3.2.1 Cohesive Zone Modeling

Compared to the VCCT the CZM approach allows a more general and physically representative approach to crack emergence and propagation modelling. CZM also has considerable advantages in terms of computational effort, since an initial crack is not required in advance as for VCCT [33]. The idea is that in front of the crack tip, a very thin layer is present, in which the damage mechanisms leading to fracture are confined. The behavior of this layer, the cohesive zone, is characterized by a traction-separation law (TSL), also called cohesive law [1]. There are several TSLs available that can be used for CZM, an example can be seen in Figure 3.8. To use the CZM in a finite element analysis, the above mentioned CEs are necessary. These elements have been developed to model adhesives, crack tips or bonded interfaces, like

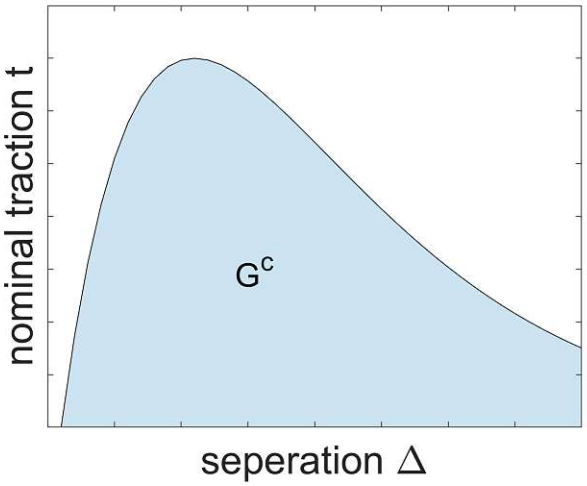

Fig. 3.8: Generic cohesive law for CZM

in composites. Compared to a continuum element, which uses a stress versus strain relationship to define its material behavior, cohesive elements are interface elements, which use a stress versus relative (opening and sliding) displacements relationship. These CZMs can also be used to model the interfaces in laminates and, e.g., predict the onset and growth of delamination due to impact. A good overview of this is given in [1]. This method will also be used to model the interfaces in this work and the kinematics of cohesive elements will therefore be presented in more detail below, before summarizing the traction separation approach.

3.3.2.2 Cohesive element kinematics

To simulate the interfaces of composites, which are usually resin-rich layers between the layers of fibers, different cohesive elements can be used. The constitutive equation of these CEs is defined by the relative displacements of the element's surfaces and the tractions across the interface. In [4] the standard formulation for a CE, as used in the commercially available FEM solver Abaqus/Standard 2023 (Dassault Systèmes/Vélizy-Villacoublay, FRA),which is used in this work, is given. The basics of this derivation will be given below.

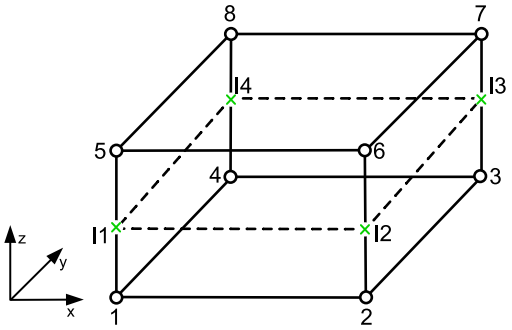

Fig. 3.9: Standard 3d 8-node CE

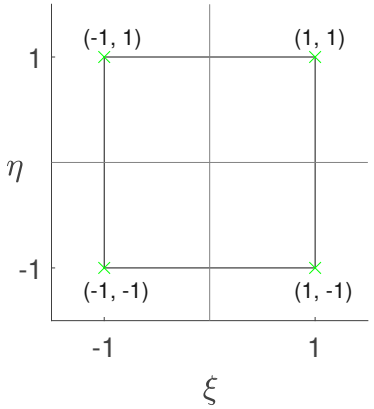

Fig. 3.10: Parent domain of CE

The geometry of an 8-node three-dimensional CE can be seen in Figure 3.9, with the elements midplane (dotted lines) and the integration points marked with green crosses. As with other finite elements, CEs can be defined as isoparametric elements. The midplane is therefore mapped to a parent domain with the coordinates ξ and η (see Figure 3.10). The relative displacements in global coordinates Δ_i of an isoparametric element can be written as

$$\Delta_i = u_i^+ - u_i^- = N_k u_{ki}^+ - N_k u_{ki}^- \tag{3.14}$$

with u_{ki}^+ and u_{ki}^- being the displacements of the top and bottom nodes k in direction i. In its standard version, the top and bottom surface of the CE are initially overlapping (zero-thickness, see [4]). The shape functions are therefore bilinear in the 2D parent domain [33], as shown in Figure 2.7 and are written as

$$N_1(\xi,\eta) = \frac{1}{4}(1-\xi)(1-\eta) \tag{3.15a}$$

$$N_2(\xi,\eta) = \frac{1}{4}(1+\xi)(1-\eta) \tag{3.15b}$$

$$N_3(\xi,\eta) = \frac{1}{4}(1+\xi)(1+\eta) \tag{3.15c}$$

$$N_4(\xi,\eta) = \frac{1}{4}(1-\xi)(1+\eta) \quad . \tag{3.15d}$$

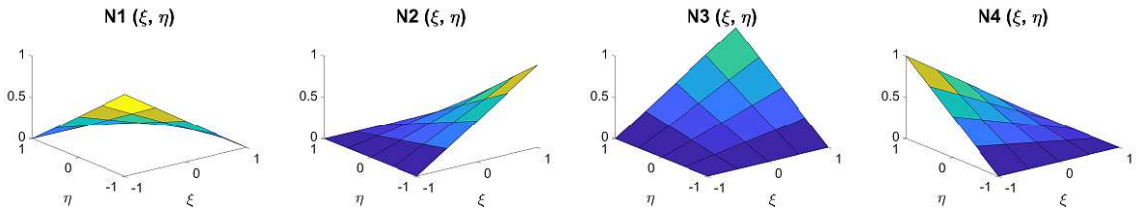

Fig. 3.11: Shape functions N_i of CE

In order to obtain the normal and tangential relative displacements for an element of general shape, Eqn.(3.14) must be transformed to local coordinates. By differentiating the global position vector $\boldsymbol{x}_i$, with respect to the local coordinates, the vectors $\boldsymbol{v}_\xi$ and $\boldsymbol{v}_\eta$ can be obtained to define the tangential plane at a given point

$$v_{\xi_i} = N_{k,\xi} x_{ki} \quad and \quad v_{\eta_i} = N_{k,\eta} x_{ki} \quad . \tag{3.16}$$

With $\boldsymbol{v}_\xi$ and $\boldsymbol{v}_\eta$ the surface normal can be defined by their vector product. This leads to the normal and tangential vectors in local coordinates (n, s, t)

$$\boldsymbol{v}_n = (\boldsymbol{v}_\xi \times \boldsymbol{v}_\eta) \parallel \boldsymbol{v}_\xi \times \boldsymbol{v}_\eta \parallel^{-1} \tag{3.17a}$$

$$\boldsymbol{v}_s = \boldsymbol{v}_\xi \parallel \boldsymbol{v}_\xi \parallel^{-1} \tag{3.17b}$$

$$\boldsymbol{v}_t = \boldsymbol{v}_n \times \boldsymbol{v}_s \quad . \tag{3.17c}$$

With $\boldsymbol{v}_n$, $\boldsymbol{v}_s$, and $\boldsymbol{v}_t$ representing the direction cosines of local to global coordinates, the transformation tensor θ_{si} is defined. This allows to transform Eqn.(3.14) in local coordinates

$$\delta_s = \theta_{si} \Delta_i = B_{sik} u_{ki} \quad , \tag{3.18}$$

where B_{sik} consists of θ_{si} and Lagrangian shape functions. The cohesive elements stiffness matrix $\boldsymbol{K}$ can be obtained with the principle of virtual work

$$\boldsymbol{K} = \int_A \boldsymbol{B}\boldsymbol{D}\boldsymbol{B}^T dA \quad . \tag{3.19}$$

Here A is the mid surface of the cohesive element and $\boldsymbol{D}$ is the element constitutive operator used to simulate the mechanical behaviour of the element, including damage mechanics. More details on this can be found in the work from Camanho and Dávila [4]. The integral is solved numerically using either the Newton-Cotes or the Gaussian integration technique. To date, no clear statement can be made about which integration scheme is best for cohesive elements. Camanho and Dávila [4] write, that Newton-Cotes is to be preferred, because Gauss quadrature in connection with cohesive elements can lead to an unwanted oscillation in the traction field, if large traction gradients are present.

Using the kinematics defined in this chapter for three-dimensional cohesive elements, in combination with a TSL, the interlaminar normal stress σ_{zz} resulting from the through thickness behavior and the interlaminar shear stresses σ_{xz} and σ_{yz} resulting from the in-plane deformations are defined. The TSL needed for this is explained in the next section.

3.3.3 Traction-separation Law

The traction-separation law is used to define the stiffness of the cohesive interface. The traction-separation model initially assumes linear elastic behavior, which corresponds to the interface's stiffness, followed by damage initiation and evolution, if defined (see Figure 3.3).

The Interfaces elastic behavior is written as

$$\boldsymbol{t} = \begin{Bmatrix} t_n \\ t_s \\ t_t \end{Bmatrix} = \begin{Bmatrix} \hat{E}_{nn} & \hat{E}_{ns} & \hat{E}_{nt} \\ \hat{E}_{ns} & \hat{E}_{ss} & \hat{E}_{st} \\ \hat{E}_{nt} & \hat{E}_{st} & \hat{E}_{tt} \end{Bmatrix} \begin{Bmatrix} \varepsilon_n \\ \varepsilon_s \\ \varepsilon_t \end{Bmatrix} = \hat{\boldsymbol{E}}\boldsymbol{\varepsilon} \quad , \tag{3.20}$$

where $\hat{\boldsymbol{E}}$ is the elastic constitutive matrix that relates the nominal stresses and nominal strains across the interface [27]. The matrix $\hat{\boldsymbol{E}}$ allows full coupling between the traction components. To ensure uncoupled traction, the off-diagonal terms must be set to zero.

The nominal traction vector $\boldsymbol{t}$ contains the nominal normal traction t_n along the local 3-direction and the nominal shear tractions t_s and t_t along the local 1- and 2-directions. The nominal strains ε_i are

$$\varepsilon_n = \frac{\delta_n}{t_0}, \quad \varepsilon_s = \frac{\delta_s}{t_0}, \quad \varepsilon_t = \frac{\delta_t}{t_0} \quad , \tag{3.21}$$

with the corresponding separations δ_i divided by the initial interface thickness t_0. The default value of the initial constitutive thickness t_0 is 1.0 in Abaqus, to ensure the nominal strain is equal to the separations if a traction-separation response is specified. The constitutive thickness used for traction-separation response is typically different from the geometric thickness (which is typically close to or equal to zero) [27]. This must be considered when defining the values for $\hat{\boldsymbol{E}}$ and is explained in section 4.1.

Chapter 4

Application of the SSA

In this chapter the implementation of the SSA in Abaqus will be explained. This requires building an FEM model with multiple layers of shell elements stacked upon each other and connecting them via cohesive elements, as explained before. In the next sections, the necessary steps to achieve this are described, with the characteristics specific to Abaqus. It also describes in detail how the stresses used for evaluation are extracted from Abaqus. After that, two use cases are introduced, where the SSA is applied to determine its performance, especially in capturing the interlaminar stresses at the free edge region of layered composites. The results are summarized and discussed in chapter 5.

4.1 SSA modelling

As described in the previous chapter, using the SSA each single ply is discretized with shell elements (Type: S4R in Abaqus) and has a thickness of t_{p}. The interfaces between the single layers are discretized with hexahedral cohesive elements (Type: COH3D8 in Abaqus) with an assigned cohesive zone approach. In order to connect the

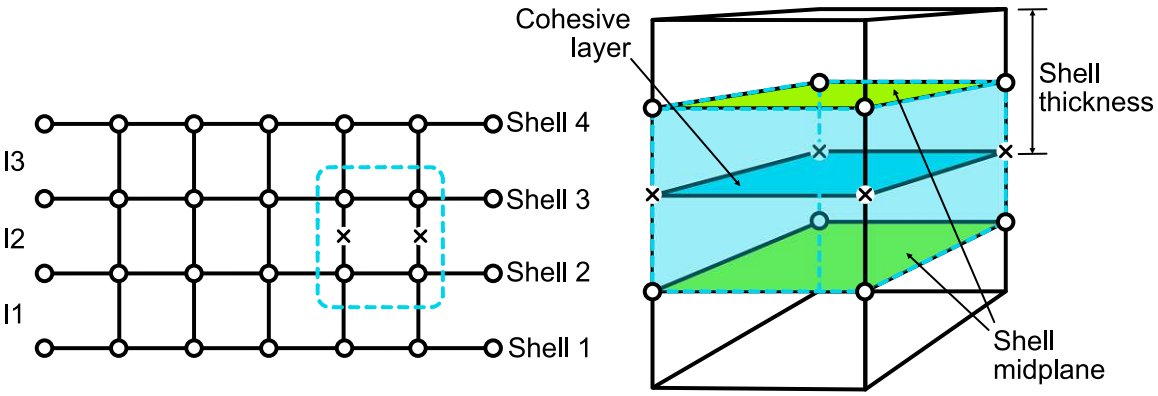

Fig. 4.1: SSA assembly of a cohesive element with two shell elements (adapted from [34])

shell element layers with the cohesive interfaces, matching meshes are used, leading to shared nodes between shell and cohesive elements. The cohesive elements geometrical thickness is defined by the distance of two adjacent shell layers. The shell offset is defined using the option middle surface (MID) in Abaqus, putting the reference surface of the shell elements in the middle of a composite layer. This leads to a geometrical thickness of the CEs of exactly one layer thickness t_p. Figure 4.1 shows the assembly of shell and cohesive elements in detail.

Considering equations (3.20) and (3.21), and that the default thickness of cohesive zones in Abaqus is $t_0 = 1$, it becomes clear that the Young's moduli used in $\hat{\boldsymbol{E}}$, to define the interface's elasticity, must be adjusted for an interface thickness not equal to 1. Equation (3.20) is therefore changed to

$$\boldsymbol{t} = \tilde{\boldsymbol{E}}\boldsymbol{\delta} \quad , \tag{4.1}$$

where $\tilde{\boldsymbol{E}}$ defines the stiffness of the interface and contains the Young's moduli from $\hat{\boldsymbol{E}}$ divided by the interface thickness, which is equal to the ply thickness t_p, coupling the tractions correctly with the CEs separations.

4.2 Stress evaluation at the free edge

To extract the stresses of the models investigated in this work from Abaqus and to display them graphically in chapter 5, Abaqus2Matlab (A2M) [19], a Matlab app in combination with Matlab is used. This section explains how the stresses are processed depending on the model and element type. In Appendix A the use of A2M is described in detail. Matlab is used to process the data from Abaqus and to plot it in a meaningful way so that the results can be interpreted.

Compared to continuum elements, stress analysis with shell and cohesive elements, as used by the SSA, requires attention to some specific features. For shell elements it is important to note that even if linear shell elements with reduced integration (S4R) have only one integration point, they may have several section points, so-called thickness integration points, depending on the settings in the section properties. In this work, the default settings in Abaqus for conventional shell sections are used. A shell element has by default five section points and only the stress values at the first (bottom) and last (top) section point are written to the output file. Per default Simpson's rule is used for thickness integration. Therefore, when displaying the results for shell elements, care has to be taken to output the stress values from the top or bottom section point, depending on the interface at which the stress values are requested. The stress values are extrapolated to the element nodes and averaged at the global nodes for each layer.

For cohesive elements, Abaqus averages the stress values across multiple interface layers, when nodal stresses are computed. For example, looking at Figure 4.2, computing the nodal stress of the node circled in red with Abaqus, will result in the averaged stress from the CEs integration points from interface 1 (I1) and interface 2 (I2). Analyzing the interface stresses in this work, this is not desirable. However, since cohesive elements are interface elements (see Section 3.3.2), and the integration points

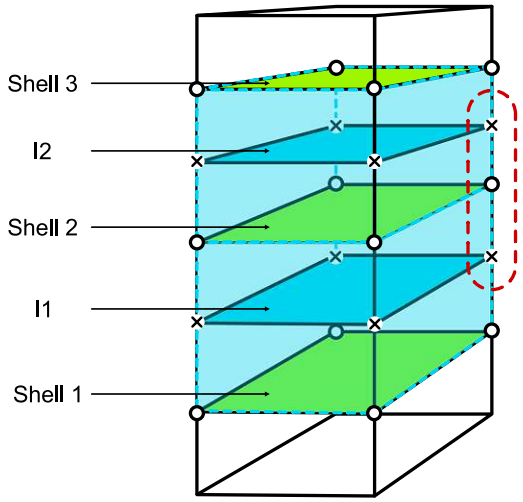

Fig. 4.2: Schematic visualization of stress evaluation for cohesive elements (COH3D8)

are located at the edges of the elements, it is permissible to directly compare the stresses from the integration points with those from the nodes of the continuum elements in the reference models. This makes it necessary to extract the stresses at the cohesive elements integration points, which can be done, e.g., with A2M. The extracted integration point stresses are only averaged with values from integration points with the same coordinates, i.e. between adjacent nodes of the same interface, and then plotted using Matlab.

For the continuum elements used in the reference models, the stresses are extrapolated from the integration points to the element nodes and averaged at the global nodes. This can be achieved with Abaqus directly, and the values are extracted and imported in Matlab via a CSV-file. Only for the interlaminar stresses of the FEE model, integration point stresses are used. As described by Norwood [14], the values of the integration points closest above and below the interface surface are taken and averaged. For this, A2M in combination with Matlab is used.

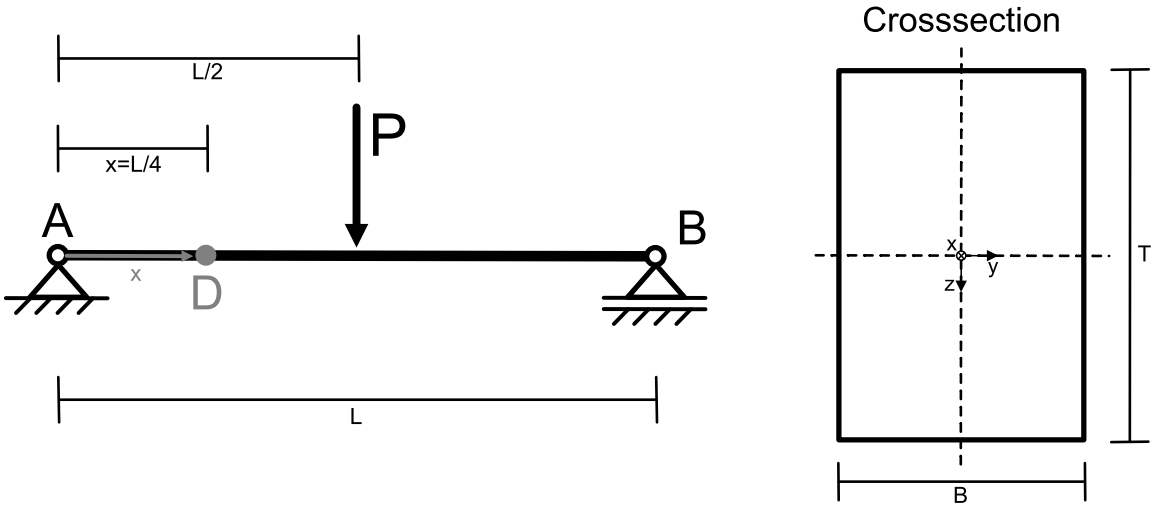

Fig. 4.3: Simulation setup for transverse shear model

4.3 Transverse shear model

To show the ability of the SSA to capture the transverse shear stresses accurately, as well as the influence of the interface properties, a three point bending test will be conducted numerically, replicating the work from Todt *et al.* [32].

The beam of the length $L = 300$ mm is loaded with the load $P = 38000$ N in z-direction at $x = L/2$. The beam is made of isotropic elastic material with a Young's modulus $E = 70000$ N/mm^2 and a Poisson's ratio $\nu = 0.33$. For the SSA models the beam is divided into $n = 40$ layers. The rectangular cross section is $B = 25$ mm wide and $T = 55$ mm high. The simulation setup is shown in Figure 4.3. The dimensions, material properties, and the load P are summarized in table 4.1. The beams deflection in z-direction along the x-axis, as well as the normal stress, and shear stresses are evaluated at $x = L/4$ (Point D) and given in chapter 5.

4.3.1 SSA model

The SSA model is built according to section 4.1. The mid-planes of the layers are discretized using 4-noded linear shell elements with reduced integration (S4R). The

Tab. 4.1: Data for transverse shear model

	Value	Unit
Length L	300	mm
Width B	25	mm
Height T	55	mm
Young's modulus E	70000	N/mm^2
Poisson's ratio ν	0.33	[−]
Load P	38000	N
Number of plies n	40	[−]
Ply thickness t_p	1.375	mm
Interface stiffness $\tilde{E}$	50909	N/mm

shell elements are assigned a homogeneous isotropic shell section with the material properties of the beam from table 4.1. The interfaces between the shell layers are discretized with cohesive elements (COH3D8) and are assigned a cohesive section with a traction-separation response. The initial thickness of the cohesive section is equal to the layer thickness ($t_\mathrm{p} = 1.375$ mm), which results from dividing the beam height H by the number of layers n. Two different SSA models are created for the transverse shear model to show the effects of the interface properties. In one, the interfaces are assumed to be rigid (i.e., the interface stiffness $\tilde{E}$ is multiplied by factor 10). In the other, the interface stiffness $\tilde{E}$ from table 4.1 (which is the Young's modulus E normalized to the interface thickness t_p) is used with a shear modulus $G = \frac{E}{2(1+\nu)}$ in order to achieve the same stiffness as for the shell element layers.

The load P is applied via a reference node whose degrees of freedom are coupled to the nodes at $x = L/2$ at the top of the beam. As boundary conditions, the degree of freedom in z-direction is locked for the nodes at the ends of the beam, and the degree of freedom in the x-direction is locked for the nodes at $x = L/2$. To obtain a statically defined problem, at each end of the beam the center node is locked in y-direction. The selected element size is 5 mm. As results, the displacements of the beam, as well as the normal, and shear stresses across the beam thickness at the location D ($x = L/4$) are presented in chapter 5.

4.3.2 Reference model

The SSA model is compared to the analytical solutions of the beam theories according to Euler-Bernoulli and Timoshenko. According to Euler-Bernoulli

$$EI\frac{\partial^4 w}{\partial x^4} = q(x) \quad , \tag{4.2}$$

with the displacement $w(x)$ of a beam due to a distributed load $q(x)$ and I being the second moment of inertia. In comparison, the theory according to Timoshenko

$$EI\frac{\partial^4 w}{\partial x^4} = q(x) - \frac{EI}{\kappa AG}\cdot\frac{\partial^2 q}{\partial x^2} \quad , \tag{4.3}$$

considers the effects of shear deformation with an additional term, where κ is the Timoshenko shear coefficient, which depends on the beams cross-section, A is the beams cross section area, and G is the shear modulus.

In addition to the analytical solutions, the SSA models are compared to a reference model made of continuum elements (C3D8). The same boundary and loading conditions, and element size are applied as for the SSA models.

4.4 Free edge effect model

To address the key question of this work, namely how well the SSA can capture the complex stress state at the free edge of layered composites, a model in which the free edge effect occurs is investigated. For this purpose, the results from Norwood [14] have been chosen for comparison. The considered layups consist of three angle-ply laminates and two cross-ply laminates and are given in table 4.2.

The investigated composite laminate is a square plate with a side length of $a = 50.8$ mm. It is loaded by a constant displacement $u = 0.508$ mm along the edge parallel to

Tab. 4.2: Investigated layups for FEE model

Layup	Stacking Sequence
A	[0/90/90/0]
B	[90/0/0/90]
C	[0/90]
D	[45/-45/-45/45]
E	[45/-45]

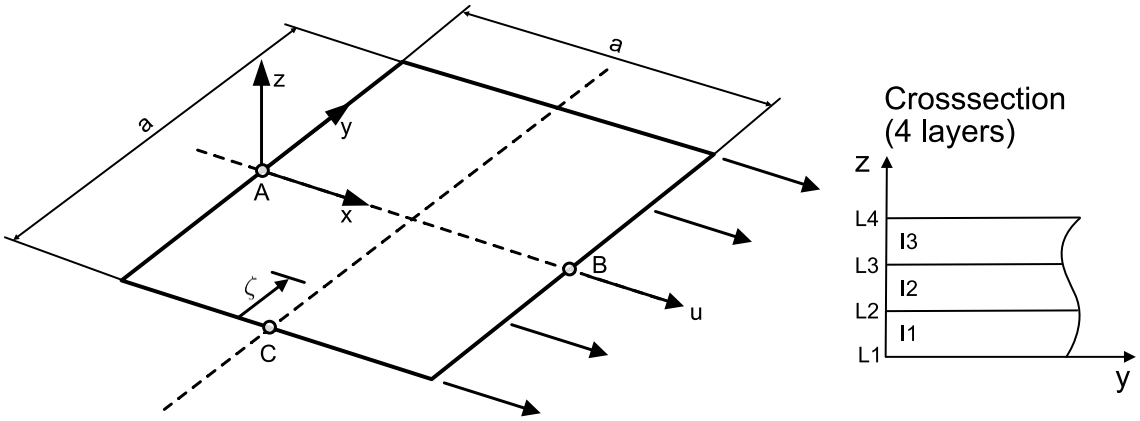

Fig. 4.4: FEE model setup and location for interlaminar stress results (adapted from [29])

Tab. 4.3: Geometric data for FEE model

	Value	Unit
Side length a	50.8	mm
Laminate thickness h	2.032/1.016	mm
Ply thickness t_p	0.508	mm
Number of Plies n	4/2	[−]
Displacement u	0.508	mm

the y-axis at $x = 50.8$ mm (Point B). Depending on the layup, the plate consists of $n = 2$, or $n = 4$ layers with a layer thickness of $t_p = 0.508$ mm each. This results in a total thickness of $h = 1.016$ mm, and $h = 2.032$ mm, respectively. The geometric data of the model is summarized in Table 4.3. A sketch is shown in Figure 4.4.

The results investigated are the stresses in the free edge region of the FEE model, starting from point C in y-direction along ζ. The in-plane stresses σ_{xx}, σ_{yy}, and σ_{xy}, as well as the interlaminar stresses σ_{zz}, σ_{xz}, and σ_{yz} at the interfaces are investigated.

In chapter 5, the results are presented and interpreted by comparing the results of the SSA model with those of the reference model. For layup A, additionally the influence of the element size on the quality of the results is investigated.

4.4.1 SSA model

As with the transverse shear model the SSA model is built according to section 4.1 and the shells are meshed with S4R elements and assigned a conventional shell section. The material data for the shells corresponds to those in Table 4.4 and are defined in Abaqus as material model of type lamina. The interfaces between the shell layers are meshed with cohesive elements (COH3D8) and are assigned a cohesive section with a traction-separation law, and have an initial thickness equal to the ply thickness ($t_\mathrm{p} = 0.508$ mm). For the cohesive section a material model of type elastic traction is defined in Abaqus. The material values of the interface are assumed to be equal to the lamina material properties perpendicular to fiber direction. Therefore, the values E_t and G_{lq} from Table 4.4 are assigned to the cohesive section, after being adjusted to the interface thickness, by dividing them with the ply thickness t_p. These interface properties are given in Table 4.5.

The displacement u is applied to the nodes at $x = a$ as a boundary condition. These nodes are also constrained in z-direction. At $x = 0$ the nodes are constrained in x- and z-direction. Additionally at both constrained edges, a node at $y = 0$ is constrained in y-direction to get a statically defined problem. The selected element size is 0.2 mm, except for layup A, models with element sizes 1 mm, 0.5 mm, and 0.25 mm are also investigated.

Tab. 4.4: Composite material data for FEE model

	Value	Unit
E_l	1.81 x10^5	N/mm^2
E_q	1.03 x10^4	N/mm^2
E_t	1.03 x10^4	N/mm^2
G_{lq}	7.17 x10^3	N/mm^2
G_{lt}	7.17 x10^3	N/mm^2
G_{qt}	3.46 x10^3	N/mm^2
ν_{lq}	0.28	[−]
ν_{lt}	0.488	[−]
ν_{qt}	0.488	[−]

Tab. 4.5: Interface material data for FEE model

	Value	Unit
$\tilde{E_{nn}}$	2.03 x10^4	N/mm
$\tilde{E_{ss}}$	1.41 x10^4	N/mm
$\tilde{E_{tt}}$	1.41 x10^4	N/mm

4.4.2 Reference model

The reference model is built according to Norwood [14] with quadratic 20-node brick elements (C3D20 in Abaqus). The material properties used are taken from Table 4.4. The continuum elements are assigned a material model of type engineering constants in Abaqus. The mesh seeding used is 0.2 mm, which leads to three elements through the thickness per layer. The same boundary and loading conditions are applied as for the SSA models.

Chapter 5

Results

In this chapter, the results of the present work are presented and interpreted. First, the results of the transverse shear model are discussed, before the results of the FEE model are presented. Especially for layup A of the FEE model the results are discussed in detail, both the influence of the mesh size and the quality of the results of the SSA at the free edge. For layups B to E, the results are summarized more concisely, since there are overlaps.

5.1 Transverse shear model

By applying the SSA approach to a transverse shear beam, the ability to capture the transverse shear stresses accurately and the effect of the interface properties can be demonstrated. As it can be seen from the beam's deflection in Figure 5.1, the SSA model with rigid interfaces behaves like an Euler-Bernoulli beam, as no deformation due to shear is captured. The SSA model with deformable interfaces behaves like a Timoshenko beam, and agrees well with the results of the continuum model.
Looking at the normal stress plotted against the beam thickness in Figure 5.2, one sees the SSA models can both capture the normal stresses with the same accuracy as

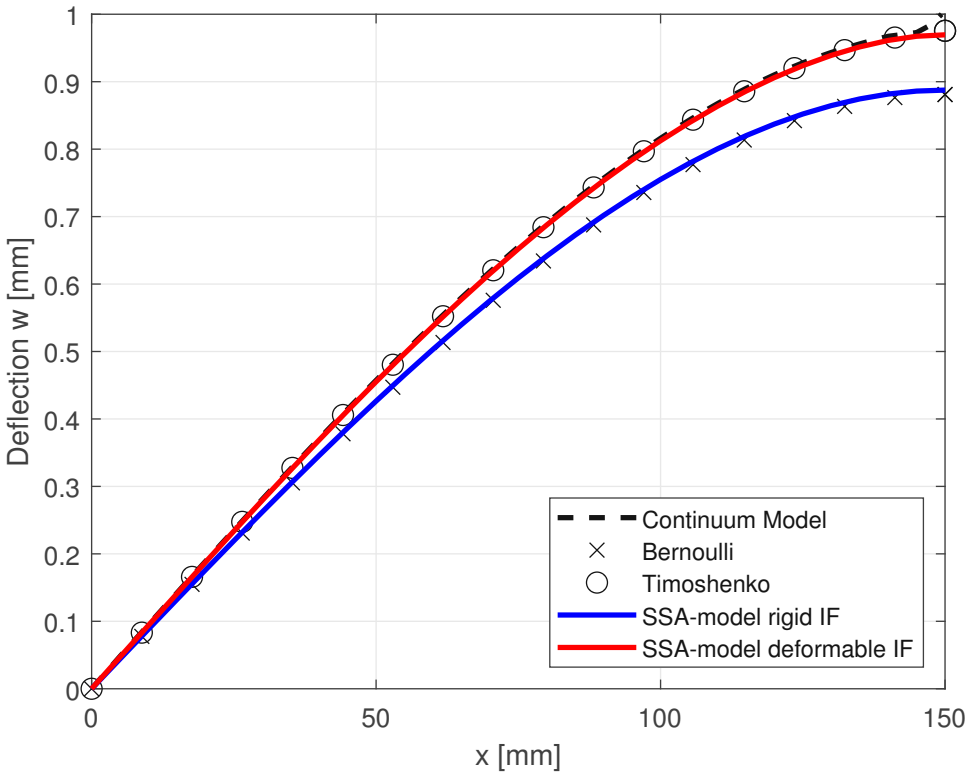

Fig. 5.1: Deflection of transverse shear beam

the continuum model, and the stiffness of the interfaces has no effect. In Figure 5.3, the transverse shear stress is plotted against the beam thickness. It can be clearly seen how important the correct interface properties are. While the values of the model with deformable interfaces agree very well with the continuum model (relative error 0.4%), the values with rigid interface deviate strongly (relative error 13.0%). The same can be seen when the shear stresses are plotted against the beam width, see Figure 5.4. The relative error for the model with deformable interfaces remains constant over the beam width at 0.4%, thus more or less following the values of the continuum model, while the relative error for the rigid interface increases from 13.0% to as much as 18.45%, showing the problems of the stiff transverse shear model. The results also agree well with the investigations of Todt *et al.* [32]. The differences regarding the shear stresses can be explained by the fact that plane-strain boundary conditions were not used in this work opposed to [32].

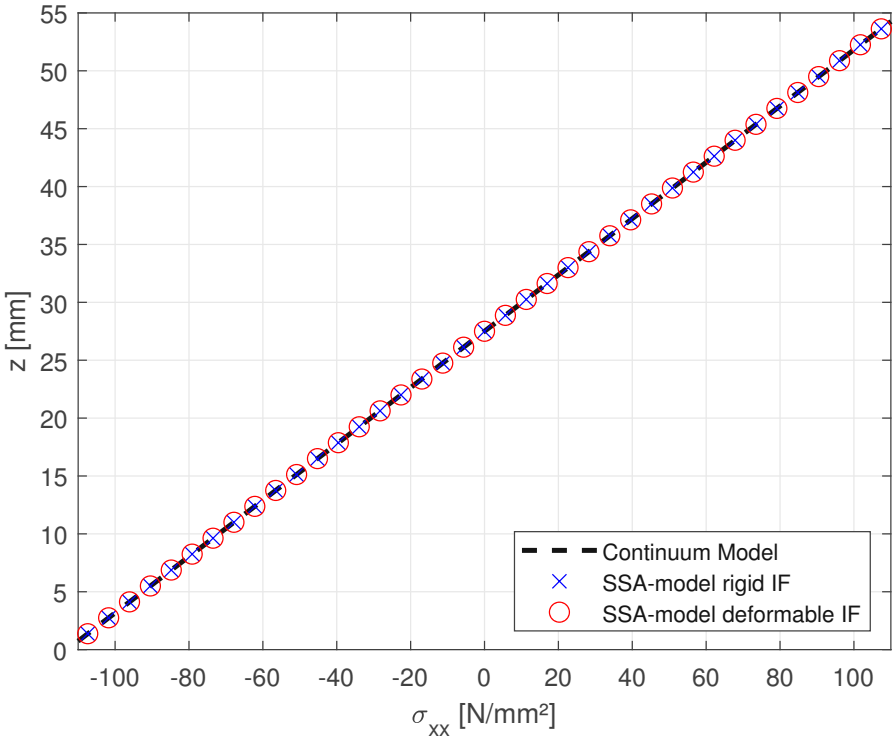

Fig. 5.2: Normal stress σ_{xx} of transverse shear beam against beam thickness at $x = L/4$

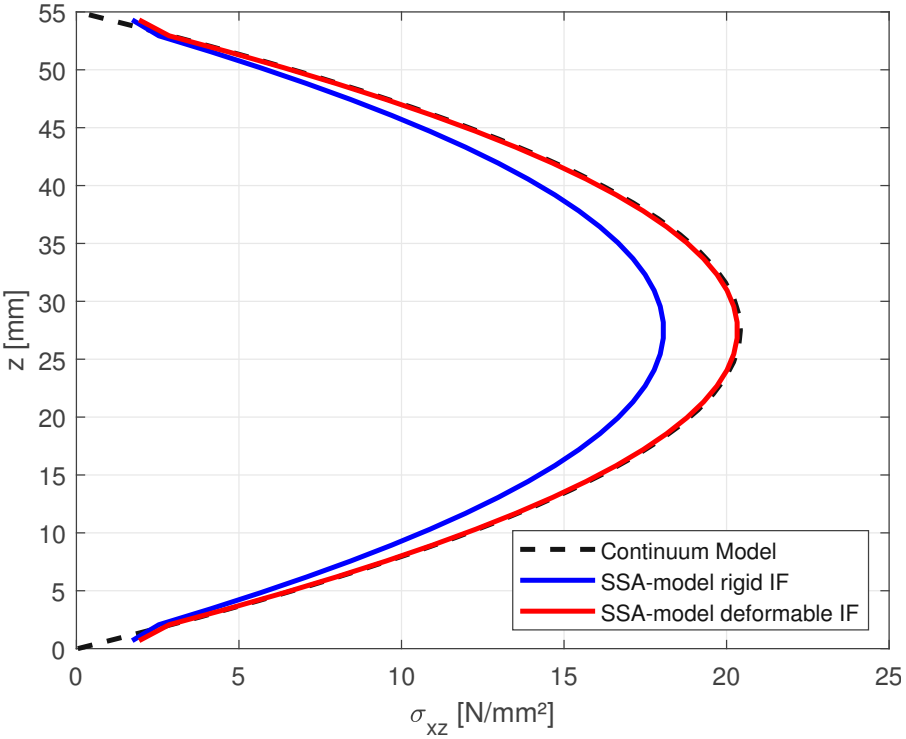

Fig. 5.3: Shear stress σ_{xz} of transverse shear beam against beam thickness at $x = L/4$

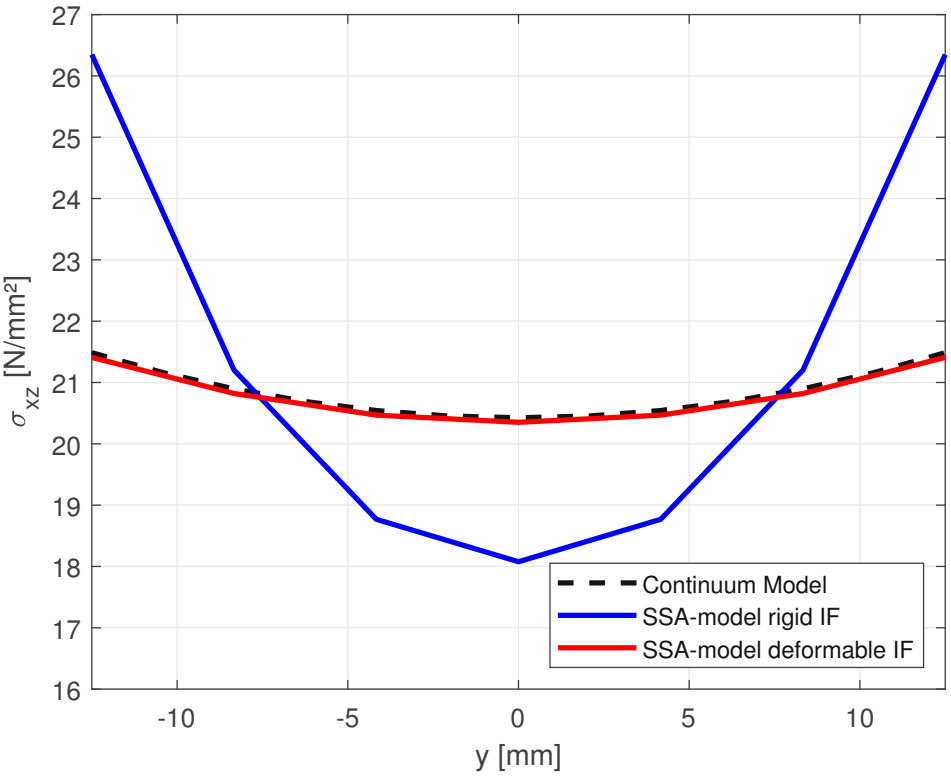

Fig. 5.4: Shear stress σ_{xz} of transverse shear beam against beam width at $x = L/4$

5.2 FEE model

In order to evaluate the ability of the SSA to capture the free edge effect in layered composites, the results of the FEE model using the SSA are compared to the results of the reference model built according to the work of Norwood [14]. The focus is on the interlaminar stresses. However, also the in-plane stresses will be compared. The results will be evaluated at the free edge, starting at Point C along ζ, see Figure 4.4. The variable ζ is normalized by two times the laminate thickness h. The results are plotted in the interval $\zeta \in [0, 1]$. All five layups given in Table 4.2 are investigated and discussed below, although the main focus is put on layup A. The results of layup A are also used to investigate the influence of the mesh size.

5.2.1 Cross-Ply Laminates

5.2.1.1 Layup A - [0/90/90/0]

Figure 5.5 shows a comparison of the interlaminar normal stress σ_{zz} at the 0/90 interface at point C as obtained by the SSA with different mesh sizes, and the reference results of [14]. The Figure shows that the results agree better and better with the reference solution as the mesh becomes finer. With matching element size of 0.2 mm, good agreement is obtained. But also the results with element size 0.25 mm provide satisfying results. The same behavior is shown in Figure 5.6, where the interlaminar stress σ_{yz} is compared, which shows that with the SSA also a coarser mesh and thus further savings in computational effort could be possible.

Norwood [14] has only published results of interlaminar stresses at one interface, but for the sake of completeness, additionally the intralaminar stresses of layers 1 and 2 at the 0/90 interface are also compared. The in-plane stress σ_{xx} at point C is shown for layers 1 and 2 in Figures 5.7 and 5.8. The results agree well up to an edge distance of approximately ply thickness t_{p}. From there the SSA is not able to capture the

effects at the free edge especially for layer 2 the differences are significant (Figure 5.8). Similar results are shown for the in-plane stress σ_{yy} in Figure 5.9. However, when comparing the SSA results for σ_{yy} with Stiftinger's [29] results, they agree well. It is therefore also conceivable that the results of the reference solution need some attention, but this is not pursued further in this work. As described above, these are not part of the evaluation of Norwood [14].

It should be noted that the results in the immediate area of the free edge are not used to evaluate the performance of the SSA. The reason for this is that linear FEM models cannot correctly represent stress singularities as they are present at the free edge. Therefore, in the Figures below, results within a distance of two elements from the free edge, which corresponds to a value of about 0.1 of $\zeta/2h$, are ignored for interpretation.

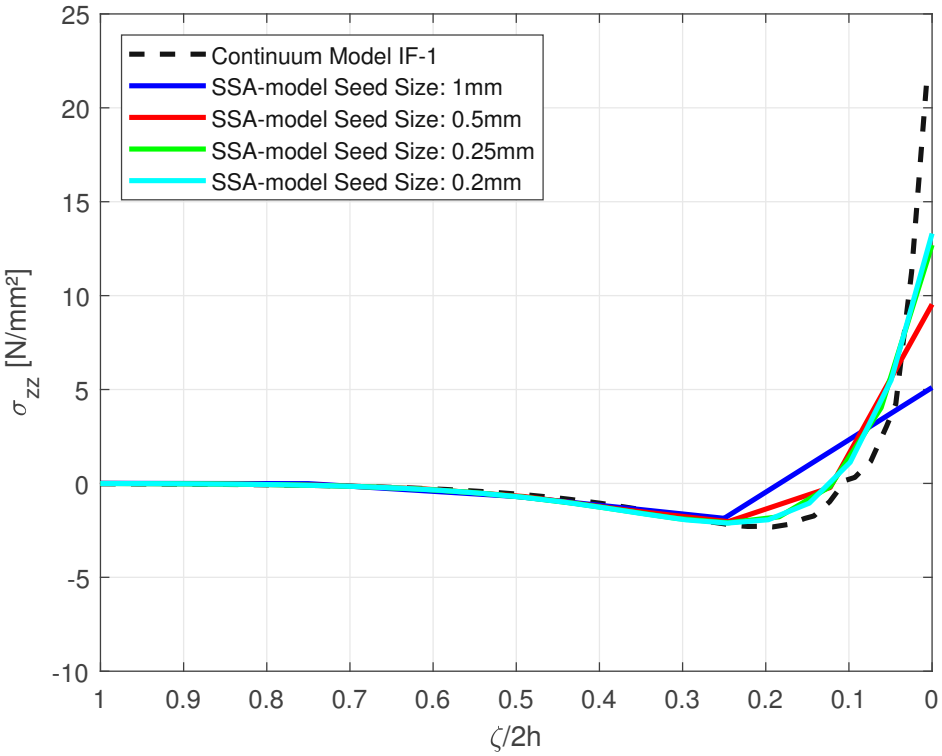

Fig. 5.5: Effect of element size for layup A - σ_{zz} at Interface 1 (0°/90°) at point C

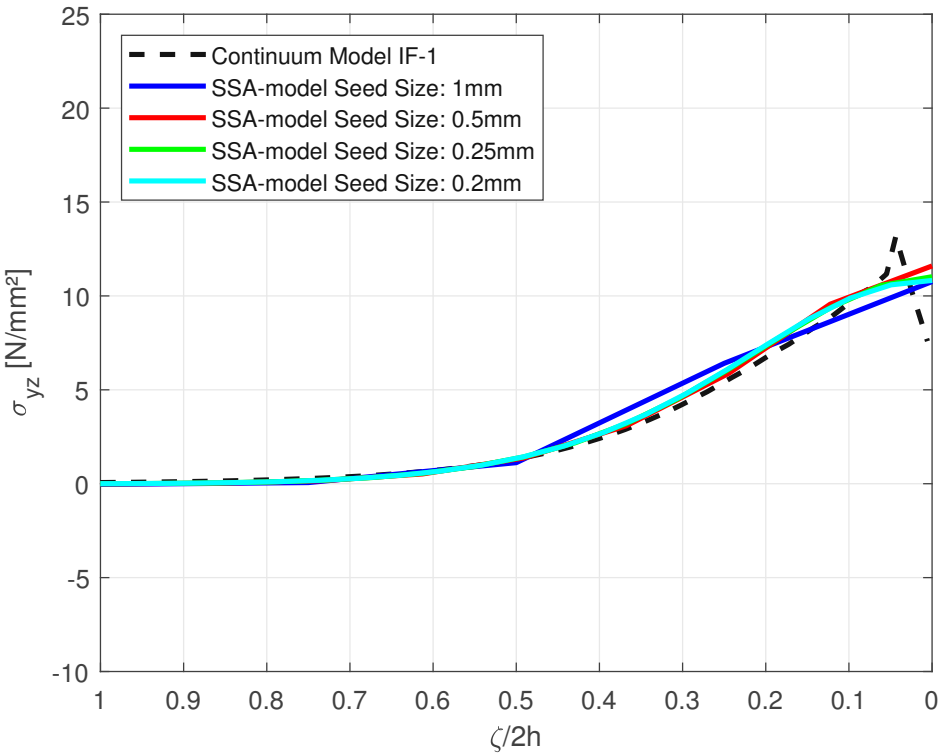

Fig. 5.6: Effect of element size for Layup A layup A - σ_{yz} at Interface 1 (0°/90°) at point C

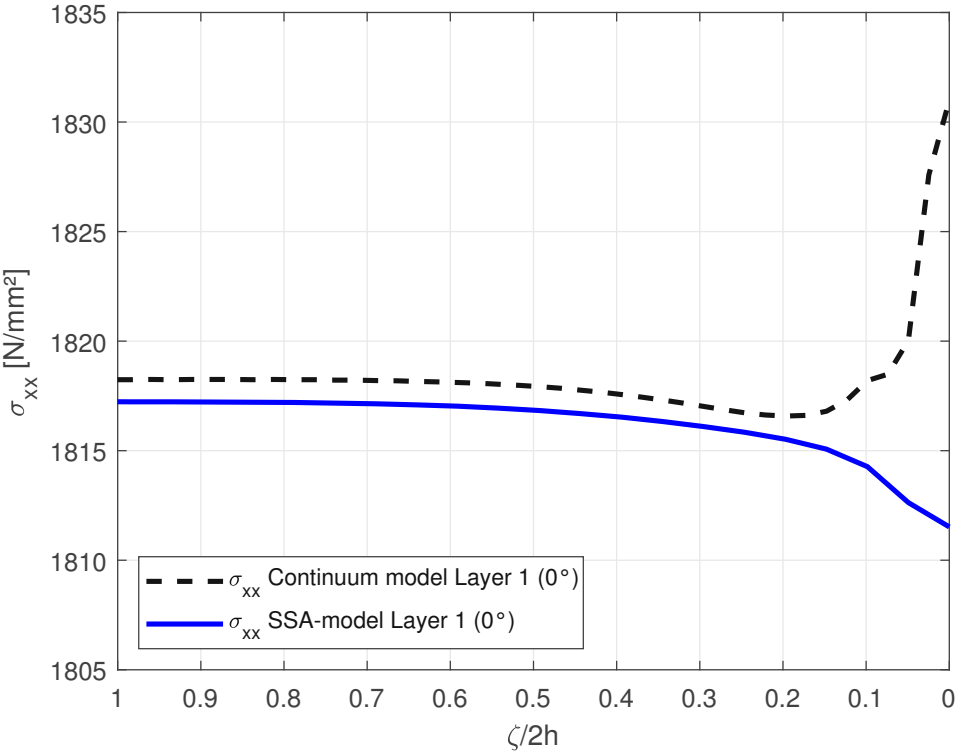

Fig. 5.7: Layup A - σ_{xx} of ply 1 (0°) at Interface 1 (0°/90°) at point C

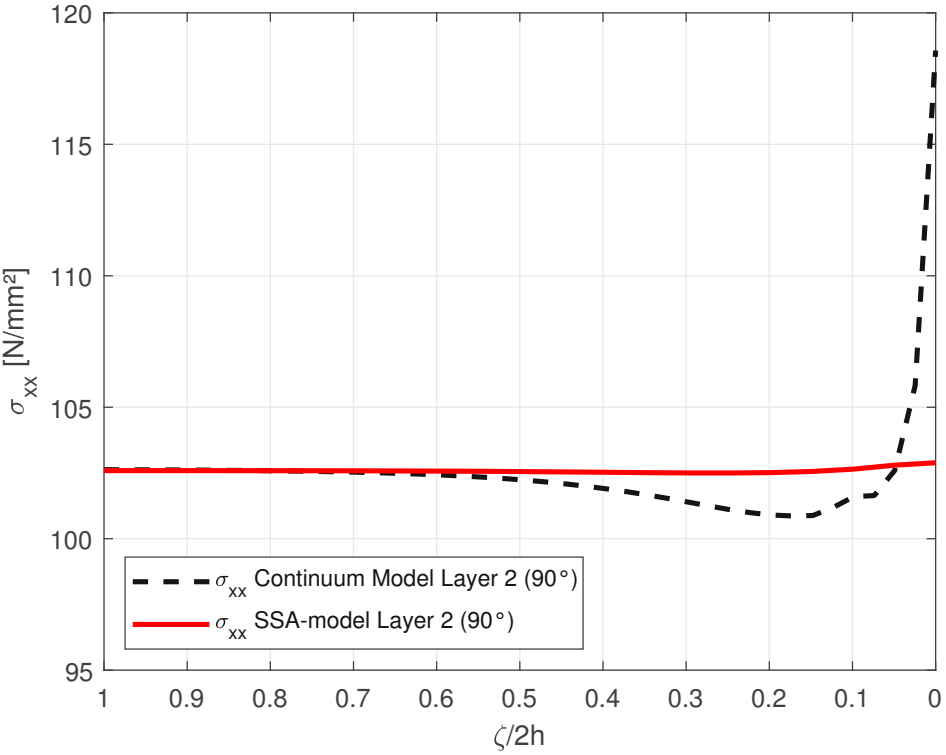

Fig. 5.8: Layup A - σ_{xx} of ply 2 (90°) at Interface 1 (0°/90°) at point C

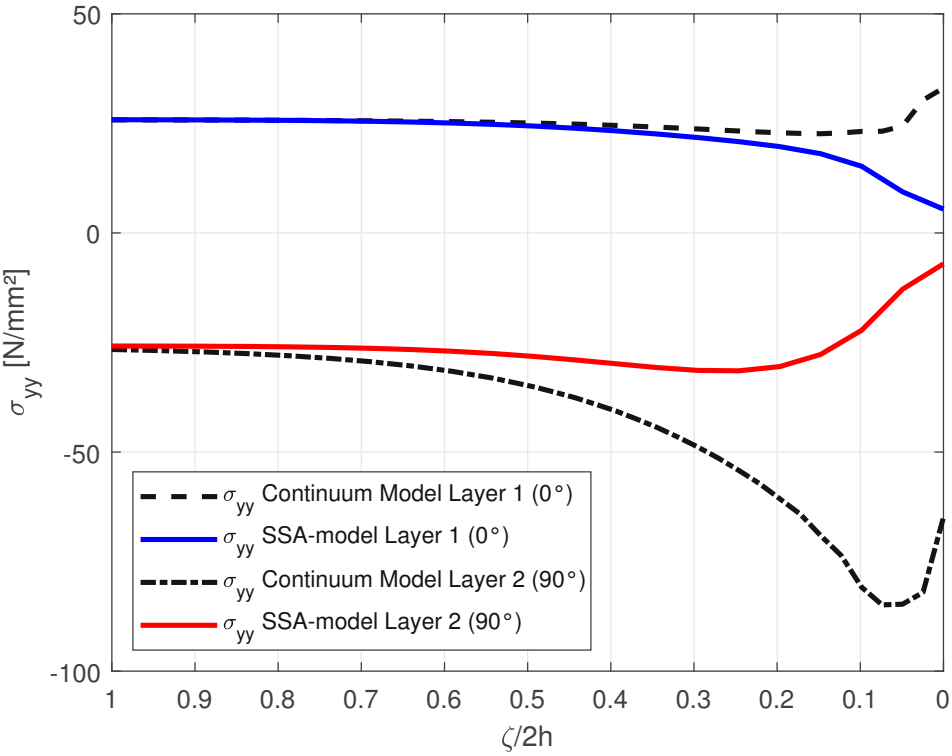

Fig. 5.9: Layup A - σ_{yy} of ply 1 and 2 at Interface 1 (0°/90°) at point C

5.2.1.2 Layup B - [90/0/0/90]

Also for layup B, the SSA gives very good results for the interlaminar stresses σ_{zz} and σ_{yz}, compared to the continuum model, as shown in Figure 5.10. It should also be mentioned that no interlaminar stress σ_{xz} is present at the free edge for the SSA, as it is correct for a layup of this type. The in-plane stresses σ_{xx} and σ_{yy} for layers 1 and 2, shown in Figures 5.11, 5.12, and 5.13, again show no agreement with the reference results. However, at least σ_{xx} of layer 2 matches in terms of quality. And also for σ_{yy} it should be noted again that the results of this work agree well with the results in [29].

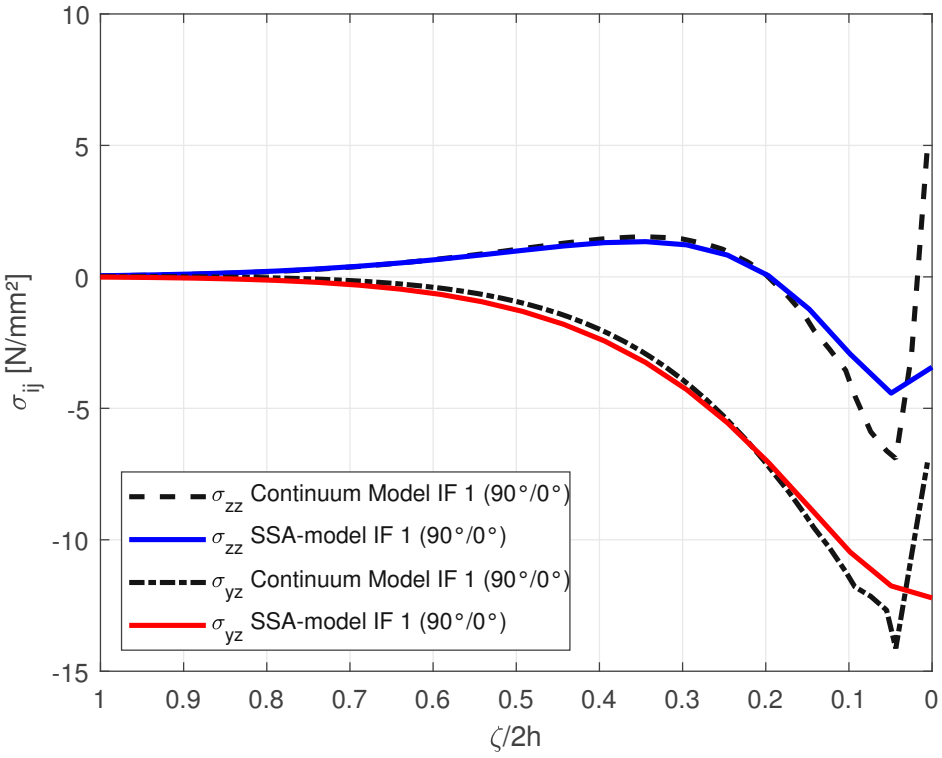

Fig. 5.10: Layup B - σ_{zz} and σ_{yz} at Interface 1 (90°/0°) at point C

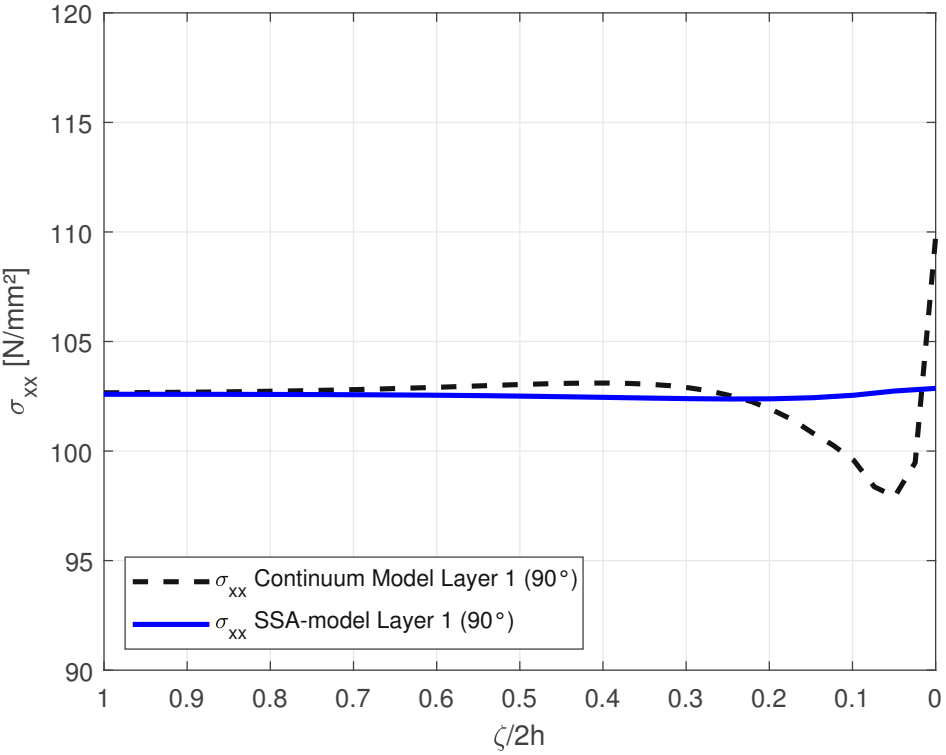

Fig. 5.11: Layup B - σ_{xx} of ply 1 (90°) at Interface 1 (90°/0°) at point C

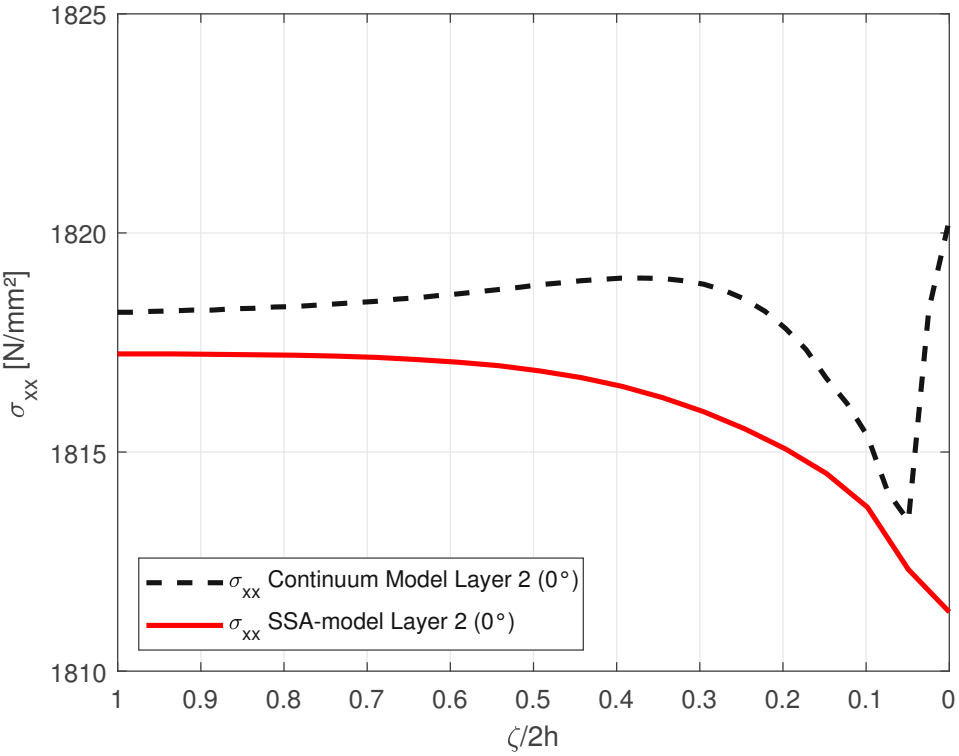

Fig. 5.12: Layup B - σ_{xx} of ply 2 (0°) at Interface 1 (90°/0°) at point C

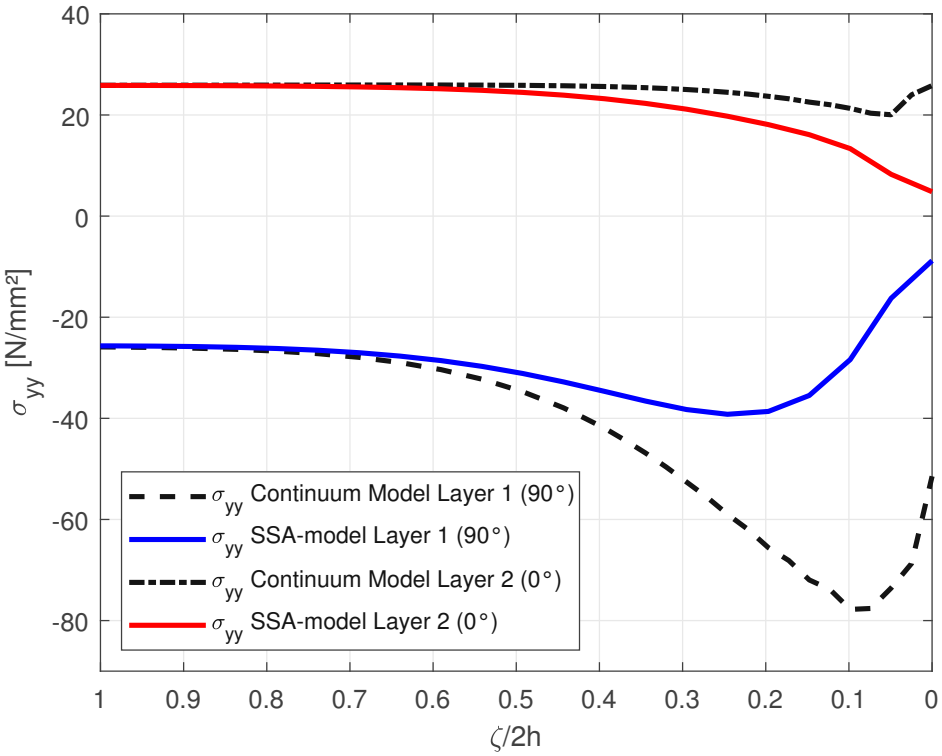

Fig. 5.13: Layup B - σ_{yy} of ply 1 and 2 at Interface 1 (90°/0°) at point C

5.2.1.3 Layup C - [0/90]

For the asymmetric cross ply layup C, the interlaminar stresses σ_{zz} and σ_{yz} are compared with the results of the reference results in Figure 5.14. The results agree well for this layup. For the in-plane stresses, the behavior is the same as for layups A and B, therefore no additional Figures are included.

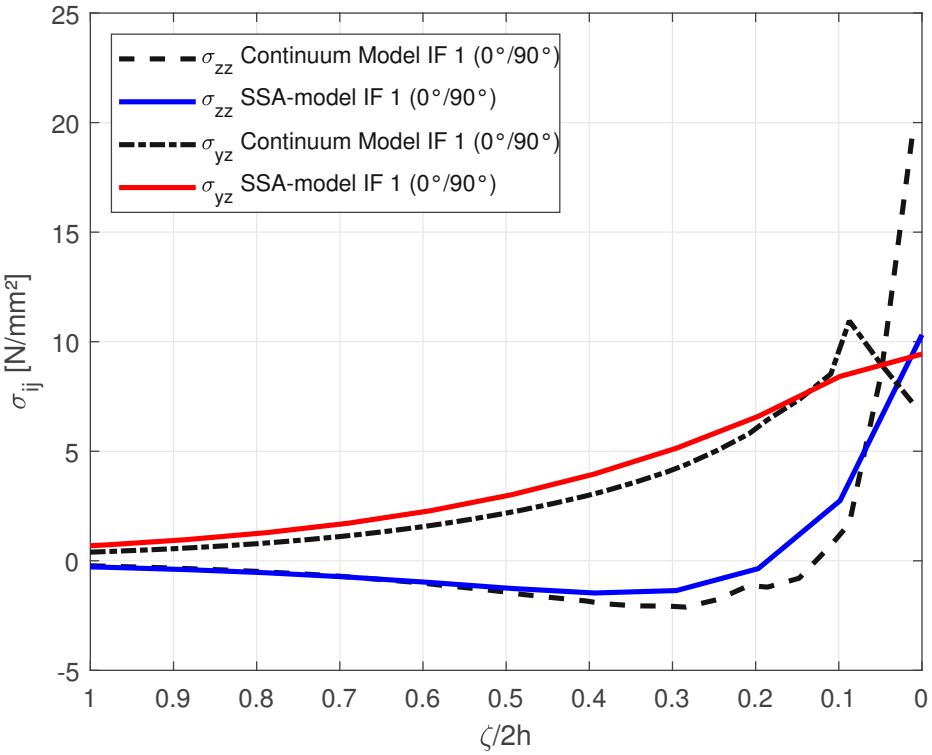

Fig. 5.14: Layup C - σ_{zz} and σ_{yz} at Interface 1 (0°/90°) at point C

5.2.2 Angle-Ply Laminates

5.2.2.1 Layup D - [45/-45/-45/45]

Figure 5.16 shows the interlaminar stresses at the $+45/-45$ interface of layup D at point C along the coordinate ζ. Compared to the cross ply layups A to C discussed before, for the angle ply layups, the interlaminar shear stress σ_{xz} does not vanish, but is the largest component of the interlaminar stresses. The results of the SSA model are in good agreement with the reference results for σ_{xz}. For σ_{zz} and σ_{yz}, shown in Figure 5.15, the SSA predicts vanishing values, exactly as in [29], and different from the reference results which show small values.

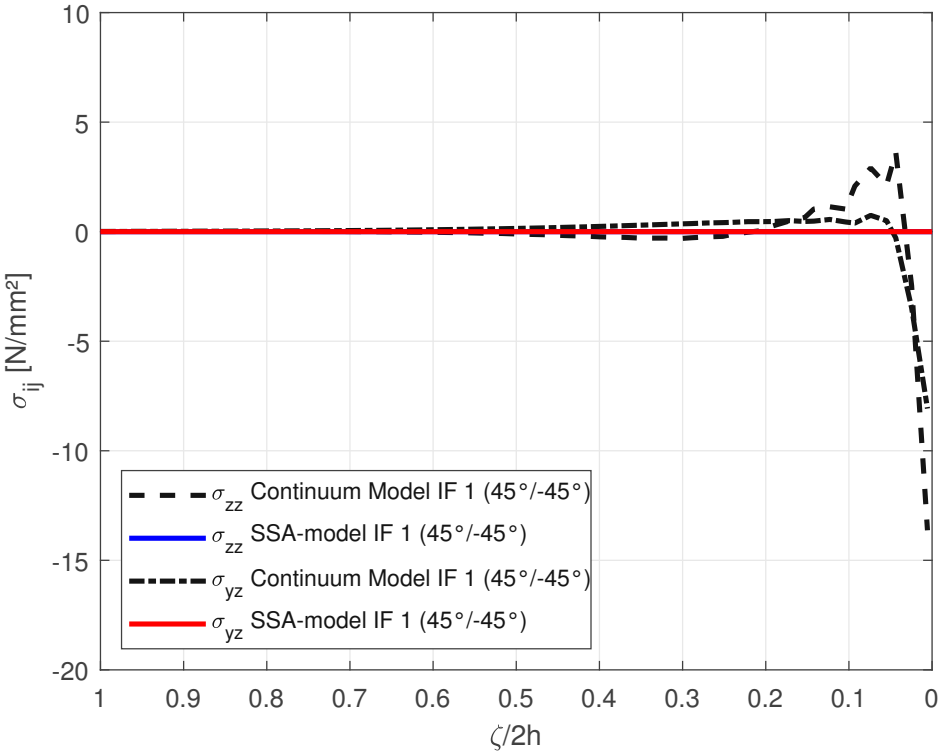

Fig. 5.15: Layup D - σ_{zz} and σ_{yz} at Interface 1 (45°/-45°) at point C

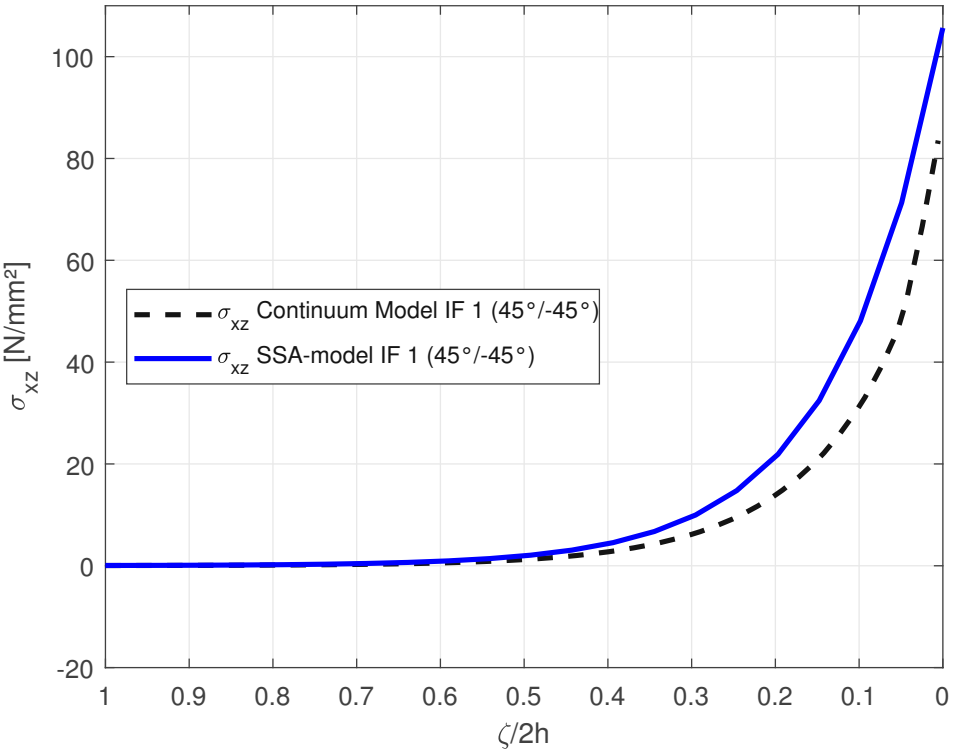

Fig. 5.16: Layup D - σ_{xz} at Interface 1 (45°/-45°) at point C

5.2.2.2 Layup E - [45/-45]

In Figures 5.18 and 5.17 the results of the interlaminar stresses of the unsymmetric cross ply layup E are plotted. Similar to layup D, the interlaminar shear stress σ_{xz} is the largest component, whereas σ_{zz} and σ_{yz} vanish for the SSA model. Again this agrees well with the results from [29], but not with the reference results, which show small values.

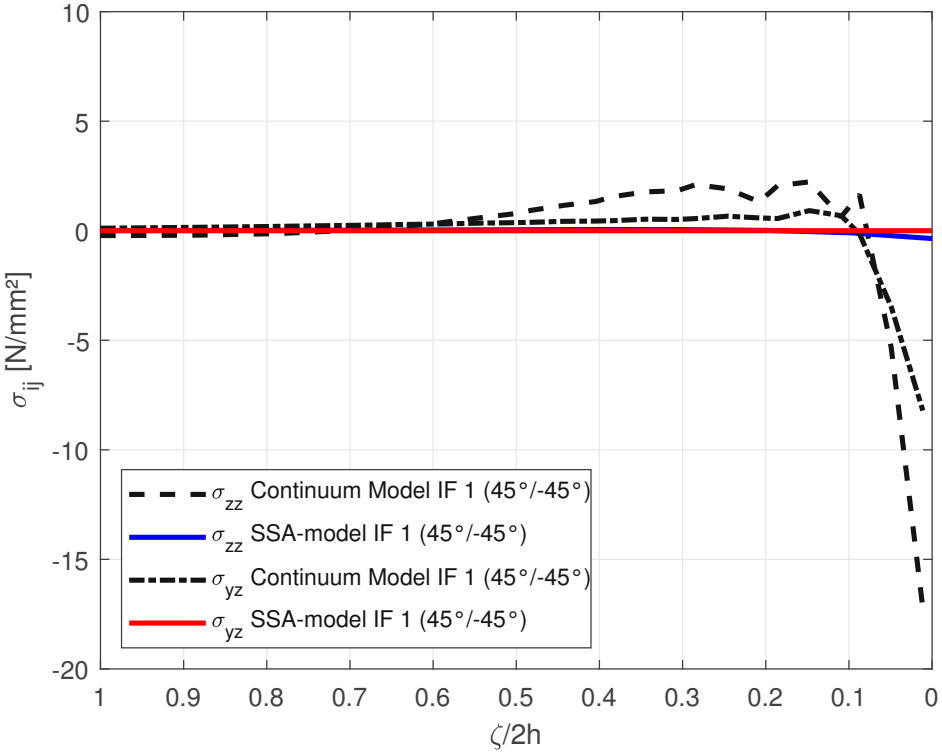

Fig. 5.17: Layup E - σ_{zz} and σ_{yz} at Interface 1 (45°/-45°) at point C

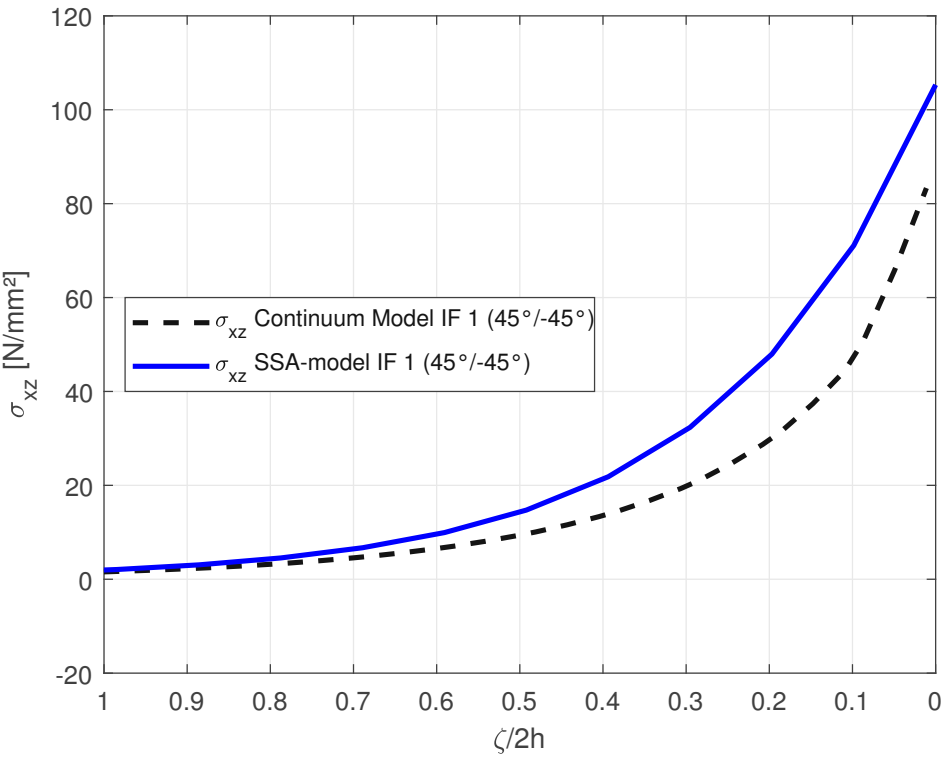

Fig. 5.18: Layup E - σ_{xz} at Interface 1 (45°/-45°) at point C

Chapter 6

Conclusion

In this thesis, the Stacked Shell Approach is used in an attempt to predict the interlaminar stresses that arise at the free edge of layered composites. This was realized by using the Stacked Shell Approach. With this approach, the individual plies of the laminate are represented by a stacking of shell element layers. Cohesive elements are used to model the interfaces between these individual shell layers. This allows the complex stress state at the free edge to be divided. The shell elements capture the in-plane stresses, while the cohesive elements capture the interlaminar stresses. The performance of the Stacked Shell Approach in capturing the interlaminar stresses at the free edge is demonstrated in two examples.

The advantage of the Stacked Shell Approach, compared to models with continuum elements, is its efficiency in computation. Using the same element size, a Stacked Shell Approach model with 4-noded linear shell elements and 8-noded cohesive elements compared to a continuum model with 20-noded hexahedral elements saves around 75% of computational effort (number of variables). Considering the results of this work, it should be possible to further increase this value, by increasing the mesh size of the Stacked Shell Approach model slightly compared to the continuum model.

Comparisons with results from calculations of continuum element models show that

the Stacked Shell Approach is able to predict the interlaminar stresses sufficiently for the investigated configurations. However, when it comes to the in-plane stresses there is still room for improvements. This might be achieved by using quadratic shell elements, or special shell element formulations. However, this would lead to a mesh incompatibility between the used cohesive elements and the shell elements. This would be the case for S8(R) shell elements, for example. Since sharing of nodes would not be possible any longer, one would have to work with ties in Abaqus, in order to connect the individual shell layers via the interfaces, which could lead to new problems.

Another option to further extend the Stacked Shell Approach would be to introduce failure mechanisms in the interfaces. This would allow to predict the onset and growth of delamination, as is briefly discussed in section 3.1.2.

In summary, the Stacked Shell Approach is able to capture the interlaminar stresses at the free edge of layered composites with good agreement compared to computationally more expensive continuum models. Considering the required computational resources it becomes clear that this is an extremely efficient and promising approach.

Appendix A

As explained in section 4.2 the outputs for this work are extracted from Abaqus by the Matlab app Abaqus2Matlab (A2M) from Papazafeiropoulos *et al.* [19] in order to import them to Matlab for plotting. To understand the necessary procedure, the process is explained below for the FEE model.

A2M is a free to use Matlab app that can be downloaded from: `https://abaqus2matlab.wixsite.com/abaqus2matlab`. For this work A2M version 3 was used. The downloaded matlab extension needs to be installed in order to work properly, an instruction as well as a video on how to install can be found on the above linked web page along with a detailed documentation.

The data, which is read into Matlab by A2M, comes from the .fil-file, the result file of Abaqus. This is not created by default, but must be forced by an extra entry in the Abaqus input file (.inp). To do this, the output request must be modified as follows in the .inp-file:

```
1 ** OUTPUT REQUESTS
2 **
3 *Restart, write, frequency=0
4 **
5 ** FIELD OUTPUT: F-Output-1
6 **
```

```
*Output, field, variable=PRESELECT
**
** HISTORY OUTPUT: H-Output-1
*FILE FORMAT, ASCII
*NODE FILE
U, COORD
*EL FILE
S
** HISTORY OUTPUT: H-Output-2
*EL FILE
COORD
*End Step
```

This generates the .fil-file with the requested output. In this case, nodal outputs for displacements (U), and coordinates (COORD), as well as element outputs, per default at the elements integration points, for stresses (S) and coordinates (COORD) are requested. The full list of available outputs can be found in the A2M documentation. The changes to the input file can be made with the A2M graphical user interface (GUI) in Matlab, the keyword editor in Abaqus, or by simply editing the input file in a text editor.

To work properly, the Matlab functions and the Abaqus .fil-file must be located in the same folder as the Matlab scripts. If you then execute the script, all functions will be processed automatically and the results will be read at the requested positions. At the end, the results are plotted and the plots are saved as vector files.

The Matlab scripts used to extract the outputs for the transverse shear and FEE models will be given to Associate Prof. Dipl.-Ing. Dr.techn. Pettermann along with the Abaqus files used for this work, allowing the work to be reproduced.

Bibliography

[1] Abrate, S., Ferrero, J. F., and Navarro, P., "Cohesive zone models and impact damage predictions for composite structures", en, *Meccanica*, vol. 50, no. 10, pp. 2587–2620, 2015.

[2] Airbus, "FAST - Special Edition A350XWB", en, *Airbus Technical Magazine*, June 2013.

[3] Barenblatt, G. I., "The formation of equilibrium cracks during brittle fracture. General ideas and hypotheses. Axially-symmetric cracks", en, *Journal of Applied Mathematics and Mechanics*, vol. 23, no. 3, pp. 622–636, 1959.

[4] Camanho, P. P. and Dávila, C. G., "Mixed-Mode Decohesion Finite Elements for the Simulation of Delamination in Composite Materials", en, *NASA/TM*, no. 2002-211737, 2002.

[5] Dugdale, D. S., "Yielding of steel sheets containing slits", en, *Journal of the Mechanics and Physics of Solids*, vol. 8, no. 2, pp. 100–104, 1960.

[6] Griffith, A. A., "The phenomena of rupture and flow in solids", en, *Philosophical Transactions of the Royal Society*, vol. 221, no. 582-593, pp. 163–198, 1921.

[7] Hein, V. L. and Erdogan, F., "Stress singularities in a two-material wedge", en, *Int J Fract*, vol. 7, no. 3, pp. 317–330, 1971.

[8] Kassapoglou, C. and Lagace, P. A., "An Efficient Method for the Calculation of Interlaminar Stresses in Composite Materials", en, *Journal of Applied Mechanics*, vol. 53, no. 4, pp. 744–750, 1986.

[9] Kassapoglou, C. and Lagace, P. A., "Closed Form Solutions for the Interlaminar Stress Field in Angle-Ply and Cross-Ply Laminates", en, *Journal of Composite Materials*, vol. 21, no. 4, pp. 292–308, 1987.

[10] Ladevèze, P., Allix, O., Deü, J.-F., and Lévêque, D., "A mesomodel for localisation and damage computation in laminates", en, *Computer Methods in Applied Mechanics and Engineering*, vol. 183, no. 1-2, pp. 105–122, 2000.

[11] Lampeas, G. and Fotopoulos, K., "Interlaminar Stresses Calculation Using a Stacked-Shell Finite Element Modeling Approach", en, *Int. J. Appl. Mechanics*, vol. 07, no. 05, pp. 155–167, 2015.

[12] Mayrhofer-Huber, B. J., "Freie-rand-effekte in laminaten", de, BA thesis, TU Wien, 2018.

[13] Mittelstedt, C. and Becker, W., "Free-Edge Effects in Composite Laminates", en, *Applied Mechanics Reviews*, vol. 60, no. 5, pp. 217–245, 2007.

[14] Norwood, D. S., "An Analysis of Interlaminar Stresses in Unsymmetrically Laminated Plates", en, Ph.D. dissertation, Virginia Polytechnic Institute and State University, 1990.

[15] Pagano, N. J., "On the Calculation of Interlaminar Normal Stress in Composite Laminate", en, *Journal of Composite Materials*, vol. 8, pp. 65–81, 1974.

[16] Pagano, N. J. and Pipes, R. B., "Some Observations on the Interlaminar Strength of Composite Laminates", en, *International Journal mechanical Science*, vol. 15, pp. 679–688, 1973.

[17] Pagano, N. J. and Pipes, R. B., "The Influence of Stacking Sequence on Laminate Strength", en, *Mechanics of Composite Materials*, vol. 5, no. 1, pp. 50–57, 1971.

[18] Pageau, S. S. and Biggers, S. B., "A finite element approach to three-dimensional singular stress states in anisotropic multi-material wedges and junctions", en, *International Journal of Solids and Structures*, vol. 33, no. 1, pp. 33–47, 1996.

[19] Papazafeiropoulos, G., Muñiz-Calvente, M., and Martínez-Pañeda, E., "Abaqus2Matlab: A suitable tool for finite element post-processing", en, *Advances in Engineering Software*, vol. 105, pp. 9–16, 2017.

[20] Pipes, R. B. and Pagano, N. J., "Interlaminar Stresses in Composite Laminates - An Approximate Elasticity Solution", en, *Journal of Applied Mechanics*, vol. 41, no. 3, pp. 668–672, 1974.

[21] Pipes, R. B. and Pagano, N. J., "Interlaminar Stresses in Composite Laminates Under Uniform Axial Tension", en, *Mechanics of Composite Materials*, vol. 4, no. 4, pp. 538–548, 1970.

[22] Rammerstorfer, F. G. and Stralinger, A., "Lamination Theory and Failure Mechanisms in Composite Shells", en, *Engineering Mechanics of Fibre Reinforced Polymers and Composite Structures*, pp. 73–110, 1994.

[23] Riener, C., "Entwicklung eines nichtlinearen finite elemente simulationsmodells zur nachbidlung des crash-verhaltens von gewebeverstärkten cfk/epoxid-laminaten", de, M.S. thesis, TU Wien, 2016.

[24] Rose, C. A. and Herakovich, C. T., "An approximate solution for interlaminar stresses in composite laminates", en, *Composites Engineering*, vol. 3, no. 3, pp. 271–285, 1993.

[25] Rybicki, E. F. and Kanninen, M. F., "A finite element calculation of stress intensity factors by a modified crack closure integral", en, *Engineering Fracture Mechanics*, vol. 9, no. 4, pp. 931–938, 1977.

[26] Schwab, M., Todt, M., and Pettermann, H. E., "Simulation of the intermediate Velocity Impact Behaviour of Woven Composite Laminates applying Progressive Damage Models for Plies and Interfaces", en, presented at the International Conference on Composite Materials, Copenhagen, 2015.

[27] Simulia, D. S. "Simulia User Assistance 2020". en. (2020), [Online]. Available: `https://help.3ds.com/2020/English/DSSIMULIA_Established/SIMULIA_Established_FrontmatterMap/DSDocHome.htm?contextscope=all` (visited on 01/18/2023).

[28] Skrna-Jakl, I., "Leichtbau mit faserverstärkten Kunststoffen", Vorlesungsskript, TU Wien, 2018.

[29] Stiftinger, M. A., "Semi-Analytical Finite Element Formulations for Layered Composite Shells with Consideration of Edge Effects", en, Ph.D. dissertation, TU Wien, 1996.

[30] Tencom. "Wind Turbine Blades: How Composites Power Green Energy". en. (2020), [Online]. Available: `https://www.tencom.com/blog/wind-turbine-blades-how-composites-power-green-energy` (visited on 06/01/2023).

[31] Teng, J. G., "Buckling of Thin Shells: Recent Advances and Trends", en, *Applied Mechanics Reviews*, vol. 49, no. 4, pp. 263–274, 1996.

[32] Todt, M., Schwab, M., and Pettermann, H. E., "Influence of interface properties on the overall elastic structural response in stacked-shell models of layered composite structures", en,

[33] Tosti Balducci, G., "C1 Cohesive Element Models for 3D Delamination", en, M.S. thesis, TU Delft, 2019.

[34] Wagner, A., "Efficient Finite Element Modelling of Residual Stresses in Multilayer Coatings", en, M.S. thesis, TU Wien, 2017.